Dynamical effect of the total strain induced by the coherent motion on local isotropy in a wake

F. Thiesset, L. Danaila, R. A. Antonia

Dynamical effect of the total strain induced by the coherent motion on local isotropy in a wake

F. THIESSET[1], L. DANAILA[1]†, AND R. A. ANTONIA[2]

[1] CORIA, Avenue de l'Université, BP 12, 76801 Saint Etienne du Rouvray, France

[2] School of Engineering, University of Newcastle, NSW 2308, Australia

(Received ?; revised ?; accepted ?. - To be entered by editorial office)

We assess the extent to which Local Isotropy (LI) holds in a wake flow for different initial conditions - these may be geometrical (the shape of the bluff body which creates the wake) and hydrodynamical (the Reynolds number)- as a function of the dynamical effects of the large-scale forcing (the mean strain $\overline{S}$ combined with the strain induced by the coherent motion, $\tilde{S}$). Local isotropy is appraised through either classical kinematic tests or phenomenological approaches. In this respect, we reanalyse existing LI criteria and formulate a new isotropy criterion based on the ratio between the turbulence strain intensity and the total strain ($\overline{S} + \tilde{S}$). These criteria involve either time-averaged or phase-averaged quantities, thus providing a deeper insight into the dynamical aspect of these flows. They are tested using hot wire data in the intermediate wake of five types of obstacles (a circular cylinder, a square cylinder, a screen cylinder, a normal plate and a screen strip). We show that in the presence of an organised motion, isotropy is not an adequate assumption for the large scales but may be satisfied over a range of scales extending from the smallest dissipative scale up to a scale which depends on the total strain rate that characterizes the flow. The local value of this scale depends on the particular nature of the wake and the phase of the coherent motion. The square cylinder wake is the closest to isotropy whereas the least locally isotropic flow is the screen strip wake. For locations away from the axis, the study is restricted to the circular cylinder only and reveals that LI holds at scales smaller than those that apply at the wake centerline. Arguments based on self similarity show that in the far-wake, the strength of the coherent motion decays at the same rate as that of the turbulent motion. This implies the persistence of the same degree of anisotropy far downstream, independently of the scale at which anisotropy is tested.

Key words: Isotropic turbulence - Wakes

1. Introduction

The analytical framework introduced by Kolmogorov (1941) for describing the properties of small-scale turbulence at sufficiently large Reynolds numbers has had a tremendous impact on turbulence research. There continues to be a strong belief among the turbulence community that if a theory of turbulence were to emerge, it would most likely relate to the small-scale motion whose features tend to exhibit quasi-universal characteristics,

† Email address for correspondence: danaila@coria.fr

e.g. Sreenivasan & Antonia (1997). Local isotropy is one of the key assumptions of the K41 theory. LI is without doubt the most utilised hypothesis, primarily because of the resulting analytical simplifications, but also because it allows experimentalists to gather only a minimal amount of information on the fluctuating velocity field. However, LI is unlikely to be satisfied reliably when a mean shear is present or in wall-bounded flows. Uniform shear flows constitute an example where even the smallest scales are affected by the large-scale shear, at least for commonly used values of the Reynolds number (Shen & Warhaft (2000)). LI also breaks down as the wall is approached, e.g. Antonia *et al.* (2009), Krishnamoorthy & Antonia (1987).

The aim of this study is to understand how, in the context of shear flows, the anisotropy propagates across the scales from the largest to the smallest, how it evolves down the scales and finally, what the degree of anisotropy is at any given scale. One of our objectives is to assess the influence of the particular nature of the flow, the differences in initial conditions and the effect of Reynolds number on local isotropy. The degree to which LI holds is quantified at a fixed position in the intermediate wake, and the return to isotropy at larger distances downstream is also investigated.

It is now recognized that the most important signature of the shear is the presence of coherent structures, which retain, through their size and dynamics, significant information about the initial conditions. For instance, the spectral slopes may be drastically affected by the presence of coherent motions (Morris & Foss (2005)). Therefore, the large-scale forcing in shear flows includes both the mean strain $\overline{S}$, as well as the strain induced by the coherent motion, $\tilde{S}$ at a fixed location in the flow. Since $\tilde{S}$ is time-dependent, a dynamical analysis of this effect on the small-scale motion is necessary. Therefore, as a first step in answering the question of what the isotropy level is at any particular scale, we consider flows populated by a single-scale, persistent coherent motion (hereafter, CM). A good candidate is the two-dimensional wake generated by different bluff bodies, and this study focuses entirely on this flow.

Several previous studies were devoted to characterising this flow, *e.g.* Antonia *et al.* (2002) (hereafter AZR), Zhou & Antonia (1994), Zhou & Antonia (1995), Antonia & Mi (1998), Kang & Meneveau (2002), etc. In AZR, both porous and impervious bodies were chosen because of the differences in the organized motion that have been observed when the shape and/or the porosity of the generators are varied (Cannon *et al.* (1993), Cimbala *et al.* (1988), Antonia & Mi (1998)). Measurements of the spanwise vorticity fluctuations ω_z were made on the centerline of the wakes generated by five different bluff bodies, *i.e.* a solid circular cylinder, a circular cylinder constructed from a screen (0.5 mm wire diameter with a mesh size of 1.6 mm), a solid square cylinder, a solid plate placed normal to the flow, and a screen strip (Fig. 1). For all of them, the characteristic dimension d (height or diameter), was the same (25.4mm). The measurements were performed at the same location ($x/d = 70$), and at nominally the same Reynolds number (R_{λ_u}, the Taylor microscale Reynolds number ≈ 200). It was emphasized that although the differences in organisation are most pronounced in the near field, they are not diminished in the far field. The global level of anisotropy, *i.e.* the ratio of the variances $\overline{v^2}/\overline{u^2}$ (u and v are respectively the longitudinal and transverse velocity components), significantly varied from flow to flow, being the largest for the screen strip and the smallest for the square cylinder. These variations were mainly due to variations in $\overline{v^2}$. AZR further showed that the autocorrelation coefficients, as well as the second-order structure functions of the velocity component v, highlighted differences among the five generators. In particular, a strong periodicity was observed for the porous body wakes at large separations. This was associated with the vortices which first appear in the mixing layers that originate from

the edges of the mesh and subsequently undergo pairing, thus increasing their intensity further downstream.

Second-order structure functions of v also reflected the way energy was injected into the large scales. Associated with significant changes in $\overline{v^2}/\overline{u^2}$ between the different wakes are appreciable variations in both the shape and magnitude of the Kolmogorov-normalised second-order structure functions over the restricted scaling range (RSR). The RSR is the range of scales over which the second-order structure functions exhibit a well-defined scaling, with a power-law exponent smaller than the asymptotic value of $2/3$. Oscillations were observed beyond the large-scale end of this RSR for the porous-body wakes. In the dissipative range, the distributions of Kolmogorov-normalised second-order structure functions of v did not appear to collapse as well as those for u, indicating departures from local isotropy. The derivative variances also emphasised departures from isotropy in each wake, with little evidence that the departure from isotropy differs perceptibly between the wakes of the porous generators and those of the impervious bodies. An overall conclusion of AZR was that the differences observed between the different wakes could not be simply ascribed to whether the wake generator is solid or porous, the shape of the generator being also important. The authors were not able to authoritatively comment on whether small-scale turbulence becomes universal at very large R_{λ_u}.

The roadmap of the paper is as follows. We extend the study of AZR, which focused on the behaviour of the flow at the wake centerline, in several significant ways. First, we address the question of local isotropy in the central region of a wake (up to a distance of 5 diameters away from the centerline) behind different types of bluff bodies, with particular emphasis on the circular cylinder. Secondly, and more especially, we observe the effect on LI of *(i)* the initial conditions (the large-scale organisation particular to each kind of generator), *(ii)* the Reynolds number, and *(iii)* the local values of $\overline{S} + \tilde{S}$.

These physical questions are addressed through two tools. The first one is analytical. Most of the tests them involve velocity increments at a given scale and thus provide a test of LI at that particular scale, including the smallest scales of the flow. The analytical toolbox involves two kinds of averaging: time-averaging, as well as phase-averaging.

The second tool is experimental and relies on hot wire measurements in several laboratory wakes. In part, we reanalyse the data of AZR (obtained at a single downstream location) by applying a wider range of LI criteria on a larger number of quantities than considered in AZR. Other measurements were performed at the CORIA, mainly for the circular cylinder, but the lateral distance y for these measurements extended to the position at which the mean strain is maximum. Details associated with the measurements are described in Section 2.

Section 3 contains two parts:

- The first is a review of the classical LI tests (Subsection 3.1), in which temporal-averaged statistics are compared to their isotropic values. These tests are mostly kinematic, but may also be based on transport equations. The scale at which these tests are applied may be either large, intermediate, or dissipative. The large-scale forcing ($\overline{S}$ and $\tilde{S}$) does not appear explicitly in most of these tests. The dynamical aspect is not tackled along conventional lines, and we indicate how this is done.
- The second deals with phenomenological LI tests (Subsection 3.2), which explicitly account for the large-scale strain, as well as its dynamical phase evolution.

Section 4 is devoted to results on the wake centerline. Isotropy tests at different scales mentioned in Section 3 are investigated experimentally. Small-scale limits of these tests are also discussed. Finally, Section 5 deals with the role of the combined action of the mean shear $\overline{S}$ and of the coherent motion strain $\tilde{S}$, on LI in the wake of a circular cylinder.

Section 6 deals with the anisotropy effects in the far field. Conclusions are drawn in Section 7.

2. Experiments

Two types of experiments have been done: the first data set concerns measurements made at the University of Newcastle in wake flows behind five types of obstacles (subsection 2.1). Subsection 2.2 deals with the description of measurements performed at the CORIA, University of Rouen, in a circular cylinder wake.

2.1. *Newcastle data set*

Measurements were performed in an open circuit wind tunnel with a 2.4m long test section ($0.35 \times 0.35\ m^2$). Five different generators were used, all of them with the same characteristic dimension $d = 25.4mm$: a circular cylinder (CC), a square cylinder (SqC), a screen cylinder (ScC), a normal plate (P) and a screen strip (SS) (Fig 1). The generators were located 20cm downstream of the entrance to the test section and spanned the full width of this section. The measurement location is $70d$ downstream of the generator, on the wake centreline. The spanwise and lateral vorticity components (ω_z, ω_y) were measured independently, by rotating a single component vorticity probe. Detailed information on the generators and the probe is given in AZR. It is sufficient to note here that all the hot wires (Pt-10% Rh) had a diameter of 2.5 μm and an active length of about 0.5 mm (length to diameter ratio $\simeq 200$). The hot wires were operated at an overheat ratio of 1.5 with constant temperature anemometers. The anemometer output signals went through buck and gain circuits, before low-pass filtering at a cut-off frequency f_c which was set very close to the Kolmogorov frequency $f_K (=U/2\pi\eta$, U is the local mean velocity and η is the Kolmogorov microscale). The filtered signals were sampled at a frequency of approximately $2f_c$ into a PC using a 12 bit A/D converter. The sampling period was in the range 45-100 s. The mean velocity U_0 of the incoming stream was varied from wake to wake to provide data in the range $150 \lesssim R_{\lambda_u} \lesssim 300$. The majority of the measurements discussed in AZR were made at approximately the same Taylor microscale Reynolds number $R_{\lambda_u} (\simeq 200)$ in each wake, at the same location $x/d = 70$. The corresponding values of U_0 were 8.8m/s for CC, 7.5 m/s for SqC, 6.2 m/s for ScC, 8.3 m/s for P and 15.1 m/s for SS.

The separation between hot wires and the sampling frequency were adjusted so that $\Delta x \approx \Delta y \approx \Delta z \approx 3 - 6\eta$, depending on the Reynolds number. Whereas a separation of 3η may be appropriate for correctly inferring derivative statistics, an attenuation of these statistics is likely with a separation of 6η. This attenuation may be estimated using the spectral correction method provided by Antonia *et al.* (1996).

Here, we briefly recall the method for a one-component vorticity probe. The ratio between the measured spectrum $P^M_{u_{,y}}$ and the true spectrum $P_{u_{,y}}$ of $u_{,y} \equiv \partial u/\partial y$ is (Antonia *et al.* (1996)):

$$\frac{P^M_{u_{,y}}}{P_{u_{,y}}} = \frac{4 \iint_{-\infty}^{\infty} \sin^2\left(\frac{k_y \Delta y}{2}\right) \frac{E(k)}{4\pi k^4} \left(k^2 - k_x^2\right) dk_y dk_z}{(\Delta y)^2 \iint_{-\infty}^{\infty} k_y^2 \frac{E(k)}{4\pi k^4} \left(k^2 - k_x^2\right) dk_y dk_z}, \tag{2.1}$$

where $k = \left(k_x^2 + k_y^2 + k_z^2\right)^{1/2}$ is the magnitude of the wave number vector (k_x, k_y and k_z are wavenumbers along the x, y and z directions respectively) and $E(k)$ is the 3D energy spectrum. Replacing y by z leads to a similar expression for $P^M_{u_{,z}}$. Note that in reality, the double integrals in Eq. (2.1) do not extend from $-\infty$ to ∞ since the integrated functions decay to zero.

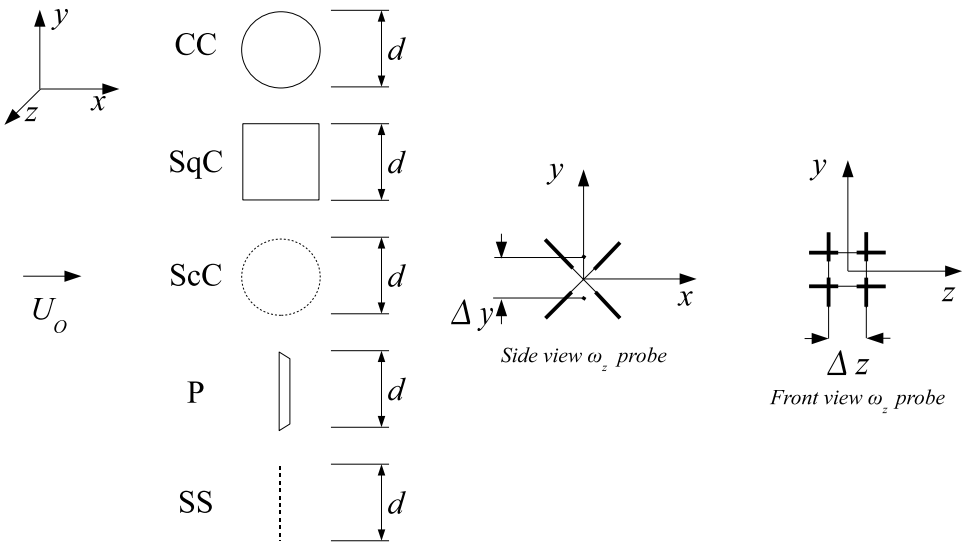

FIGURE 1. Cross section of the five different generators. From top to bottom: CC, SqC, ScC, P, SS. Also sketched is a one-component vorticity probe in the ω_z configuration (ω_z is the vorticity component in the z direction).

	λ_u (mm)			$\bar{\epsilon}$ $(m^2.s^{-3})$			R_{λ_u}		
CC	6.39	5.30	3.91	0.98	2.47	14.26	164	188	252
SqC	5.78	5.12	3.81	1.74	3.01	20.57	183	197	286
ScC	5.79	5.25	3.54	1.34	2.74	23.94	178	198	255
P	5.69	4.83	3.50	1.46	3.39	22.24	156	186	247
SS	5.29	4.52	3.47	0.88	2.44	14.78	114	140	197

TABLE 1. Values of the Taylor microscale λ_u, $\bar{\epsilon}_{iso}$ and the Taylor microscale Reynolds number R_{λ_u} for the five different generators.

For the longitudinal derivatives, the measured spectrum $E^M_{u,x}$ is related to the true spectrum $P_{u_{,x}}$ via the sinc function, *viz.*:

$$\frac{P^M_{u_{\alpha,x}}}{P_{u_{\alpha,x}}} = \mathrm{sinc}^2\left(\frac{k_x \Delta x}{2}\right), \tag{2.2}$$

where $u_\alpha \equiv u, v, w$. It is important to recall that while LI is invoked in Eq. (2.1), the correction of any streamwise derivative spectrum (Eq. (2.2)) does not require this assumption. Nor is a knowledge of $E(k)$ necessary.

Measurements were performed at three values of the Taylor microscale Reynolds number R_{λ_u}, based on the RMS of u and the Taylor microscale ${\lambda_u}^2 = 15\nu\frac{\overline{u^2}}{\bar{\epsilon}}$. The Taylor microscale λ_u, the isotropic mean energy dissipation rate $\bar{\epsilon}_{iso} = 15\nu\overline{\left(\frac{\partial u}{\partial x}\right)^2}$ and the Taylor micro-scale Reynolds number for each generator are reported in Table 1, for each generator. Note that $\overline{\left(\frac{\partial u}{\partial x}\right)^2}$ was corrected using Eq. (2.2).

2.2. *CORIA data set*

The wind tunnel is of the recirculating type with a residual turbulence level smaller than 0.2 %. The test section is $0.4 \times 0.4\ m^2$ and 2.5m long and the mean pressure gradient was adjusted to zero. The circular cylinder of diameter $d = 10mm$ was placed horizontally, downstream the contraction, spanning the whole test section. The upstream velocity was $U_0 = 6.5m.s^{-1}$ corresponding to a Reynolds number based on the cylinder diameter of 4333 and a Taylor microscale Reynolds number of 70. Measurements were made at 70d downstream of the cylinder and for transverse positions varying between $y = 0$ and $y = 5d$.

Only the streamwise and transverse velocity components u and v were measured. The X-wire probe (Dantec 55P51) was calibrated using a look-up table technique, with velocity increments of 1 m/s and angle increments of 5^0. The hot wires were operated by a Dantec constant temperature bridge, with an overheat ratio of 1.6. Voltage signals were passed through amplifiers (SRS SIM983) and low-pass filtered (SRS SIM965) at a frequency close to the Kolmogorov frequency. The air temperature in the wind tunnel was kept constant during calibration and measurements, thus avoiding any systematic errors that slight variations in the mean temperature could induce on hot wire voltages.

3. Description of the analytical tools. LI tests at different scales

This section provides an overview of the analytical tests used in this paper. They are either kinematic (Subsection 3.1) or phenomenological (Subsection 3.2). In each subsection, both time-averaged and phase-averaged quantities are considered.

3.1. *Kinematics LI tests*

3.1.1. *Time-averaged quantities*

We present here LI tests at any scale r, with particular emphasis on the range of scales where a scaling law can be defined, if any, the RSR. For relatively high Reynolds numbers, the scaling laws tend to the asymptotic values of '2/3' for the structure function, and the RSR is identified with an Inertial Range (IR).

Following Monin & Yaglom (2007), the well-known isotropic relation between second-order structure functions of the longitudinal velocity components and those of the transverse velocity components ($u_\perp$) is given by

$$\overline{(\Delta u_\perp)^2}|_{iso} = \left(1 + \frac{r}{2}\frac{d}{dr}\right)\overline{(\Delta u)^2}, \tag{3.1}$$

where r is the separation between the point x and the point $x^+ = x + r$ and $\overline{(\Delta u_\alpha)^2} = \overline{\left(u_\alpha\left(x + r\right) - u_\alpha\left(x\right)\right)^2}$ (no summation over Greek double indices). The equivalent relation in the spectral space is

$$P_{u_\perp}(k_x) = \frac{1}{2}\left(1 - k_x\frac{\partial}{\partial k_x}\right)P_u, \tag{3.2}$$

where P_u is the power spectral density of u and k_x the streamwise wave number.

Further, it is straightforward to derive an 'isotropic' expression for $\overline{(\Delta q)^2} = \overline{\Delta u_i \Delta u_i}$ (the summation convention applies to Latin indices), *viz.*

$$\overline{(\Delta q)^2}|_{iso} = \overline{(\Delta u)^2} + 2\overline{(\Delta u_\perp)^2}|_{iso}. \tag{3.3}$$

The limits at the largest scales of (3.1) and of (3.3) yield

$$\lim_{r\to\infty}\left(\overline{(\Delta u_\perp)^2}|_{iso}\Big/\,\overline{(\Delta u_\perp)^2}\right)=\overline{u^2}\Big/\,\overline{u_\perp^2};\tag{3.4}$$

$$\lim_{r\to\infty}\left(\overline{(\Delta q)^2}|_{iso}\Big/\,\overline{(\Delta q)^2}\right)=3\overline{u^2}\Big/\,\overline{q^2}.\tag{3.5}$$

This is consistent with the 'global' isotropic ratios $\overline{u^2}/\overline{u_\perp^2}$ and $3\overline{u^2}/\overline{q^2}$ ($\overline{q^2}=\overline{u_iu_i}$ is twice the turbulent kinetic energy).

Moreover, by applying the limit as r goes to zero of (3.1) and (3.3) and since

$$\lim_{r\to 0}\left(\frac{\overline{(\Delta u_\perp)^2}|_{iso}}{r^2}\right)=2\frac{\overline{(\Delta u)^2}}{r^2}=2\overline{\left(\frac{\partial u}{\partial x}\right)^2},\tag{3.6}$$

together with the notations

$$K_1=2\overline{\left(\frac{\partial u}{\partial x}\right)^2}\Big/\,\overline{\left(\frac{\partial v}{\partial x}\right)^2}\qquad K_2=2\overline{\left(\frac{\partial u}{\partial x}\right)^2}\Big/\,\overline{\left(\frac{\partial w}{\partial x}\right)^2},\tag{3.7}$$

it can be readily shown that

$$\lim_{r\to 0}\left(\overline{(\Delta u_\perp)^2}|_{iso}\Big/\,\overline{(\Delta u_\perp)^2}\right)=2\overline{\left(\frac{\partial u}{\partial x}\right)^2}\Big/\,\overline{\left(\frac{\partial u_\perp}{\partial x}\right)^2}=K_1\quad\text{if}\quad u_\perp=v;$$
$$=K_2\quad\text{if}\quad u_\perp=w,\tag{3.8}$$

whereas

$$\lim_{r\to 0}\left(\overline{(\Delta q)^2}\Big/\,\overline{(\Delta q)^2}|_{iso}\right)=\frac{1}{5}\left(1+2K_1+2K_2\right).\tag{3.9}$$

The individual isotropic ratios K_1 and K_2, which must be equal to 1 (Taylor (1935)) in the context of LI, and represent by themselves LI tests, are therefore retrieved in the limit of small separation. Hence, the isotropic relation between second-order structure functions of different normal velocity components, but also of their sum, allows us to assess the departure from LI at any scale.

The isotropic relation between third-order structure functions is (Monin & Yaglom (2007)):

$$\overline{\Delta u(\Delta u_\perp)^2}|_{iso}=\frac{1}{6}\frac{d}{dr}r\overline{(\Delta u)^3},\tag{3.10}$$

Since at the smallest scales, $\frac{\overline{(\Delta u)^3}}{r^3}\to\overline{\left(\frac{\partial u}{\partial x}\right)^3}$ and $\frac{\overline{\Delta u(\Delta u_\perp)^2}|_{iso}}{r^3}\to\frac{2}{3r^3}\overline{(\Delta u)^3}$, and with the notations

$$G_1=\overline{\frac{\partial u}{\partial x}\left(\frac{\partial v}{\partial x}\right)^2}\Big/\,\frac{2}{3}\overline{\left(\frac{\partial u}{\partial x}\right)^3}\qquad G_2=\overline{\frac{\partial u}{\partial x}\left(\frac{\partial w}{\partial x}\right)^2}\Big/\,\frac{2}{3}\overline{\left(\frac{\partial u}{\partial x}\right)^3},\tag{3.11}$$

the small-scale limit of Eq. (3.10) yields

$$\lim_{r\to 0}\left(\overline{\Delta u(\Delta u_\perp)^2}\Big/\,\overline{\Delta u(\Delta u_\perp)^2}|_{iso}\right)=\overline{\frac{\partial u}{\partial x}\left(\frac{\partial u_\perp}{\partial x}\right)^2}\Big/\,\frac{2}{3}\overline{\left(\frac{\partial u}{\partial x}\right)^3}$$
$$=G_1\quad\text{if}\quad u_\perp=v$$
$$=G_2\quad\text{if}\quad u_\perp=w.\tag{3.12}$$

If LI was valid, the values of G_1 and G_2 must be equal to 1. Antonia *et al.* (1997) reported values of G_1 and G_2 in the wake of a circular cylinder.

Equation (3.10) leads to

$$\overline{\Delta u(\Delta q)^2}|_{iso} = \overline{(\Delta u)^3} + 2\overline{\Delta u(\Delta u_\perp)^2}|_{iso}. \tag{3.13}$$

As discussed by e.g. AZR and Shen & Warhaft (2000), the flow symmetry with respect to the wake centerline requires

$$\overline{(\Delta u_\perp)^3} = 0, \tag{3.14}$$

for each separation r. The limit at $r \to 0$ of the normalised third-order moment is the skewness of velocity derivatives, *viz.*

$$\lim_{r\to 0} \overline{(\Delta u_\perp)^3} \Big/ \left[\overline{(\Delta u_\perp)^2}\right]^{3/2} = \overline{\left(\frac{\partial u_\perp}{\partial x}\right)^3} \Big/ \left[\overline{\left(\frac{\partial u_\perp}{\partial x}\right)^2}\right]^{3/2} = S^3_{u_\perp,x}. \tag{3.15}$$

These are not LI tests, but rather symmetry tests. We expect that these relations would not be valid in the sheared region, away from the wake centerline.

Equation (3.1) has often been used to check LI in several studies (Danaila *et al.* (2001), Gotoh *et al.* (2002), Lavoie *et al.* (2005)). Its equivalent in spectral space, Eq. (3.2), has also been widely tested by *e.g.* Champagne *et al.* (1970), Mestayer (1982), Kim & Antonia (1993), Saddoughi & Veeravalli (1994). However, Eq. (3.10) has received much less attention (Gotoh *et al.* (2002)). Its limiting form as r goes to zero (*e.g.* Champagne (1978)) has been tested in a few flows (*e.g.* Antonia *et al.* (1997)).

A worthwhile exercise would be to test LI using higher-order moments than considered here and thus extend our analysis to fourth-order, or higher-order statistics. The latter may represent refined LI tests which capture departures from LI more and more effectively as the order of the statistic increases (Shen & Warhaft (2000)). Phan-Thien & Antonia (1994) tackled this problem and Ould-Rouis *et al.* (1996) empirically extended the results to structure functions. However, there are doubts concerning the validity of their results. Indeed, Phan-Thien & Antonia (1994) characterized the *8-th* order moment tensor by means of a single invariant whereas Siggia (1981) suggested that at least four invariants are needed. Hierro & Dopazo (2003) obtained a more compact expression (for the *8-th* order moment tensor) than - though in full agreement with - that of Siggia (1981); they also concluded that their expression was more accurate than the simpler expression of Phan-Thien & Antonia (1994). Nevertheless, Hierro and Dopazo's result needs to be fully tested, especially in the light of the limited experimental evidence in grid turbulence (Zhou & Antonia (2000)) that the four invariants seem to be related. We limit the present study to second- and third-order structure functions partly because reliable relations for fourth-order structure functions are not yet available.

3.1.2. *Phase-averaged quantities*

Let us now consider the dynamical aspect of the statistics. Although most of the previous investigations have dealt with the total velocity field, we recall that fluctuating, quasi-periodic contributions are present in the flow, notably for the v component. In order to understand the role of the coherent motion and its strain on LI, the next step is to adopt a different viewpoint.

To this end, any quantity β is decomposed according to $\beta = \overline{\beta} + \tilde{\beta} + \beta'$ where $\tilde{\beta}$ denotes the periodic contribution associated with the coherent motion and β' is the random/turbulent fluctuation, while $\overline{\beta}$ is the time-averaged component. One way to calculate $\tilde{\beta}$ is to perform phase-averaging over the period of the coherent motion (Reynolds & Hussain (1972)). Hereafter, phase-averages will be denoted $\langle . \rangle$. Applying a phase aver-

age to the quantity β leads to $\langle\beta\rangle = \overline{\beta} + \tilde{\beta}$ since the phase-averaged random component vanishes, *i.e.* $\langle\beta'\rangle = 0$.

Phase-averaged statistics are obtained as follows. The transverse velocity component v is first digitally band-pass filtered at the peak frequency of the v spectrum, using an eighth-order Butterworth filter. The filtering operation is next applied to the Fourier transform of v in order to avoid any phase shift. Then, the Hilbert transform h of the filtered signal v_f is obtained and the phase ϕ inferred from the relation $\phi = \arctan\left(\frac{h}{v_f}\right)$. Hereafter, the symbol ϕ indicates the phase of the flow. Finally, the phase is divided into 21 segments and phase-averaged statistics are calculated for each class. The convergence of statistics was checked, by reducing the number of classes, and found to be satisfactory. By means of this method, phase-averaged quantities are calculated over the period $[-\pi, \pi]$. As was done by O'Neil & Meneveau (1997), the phase is doubled up to $[-2\pi, 2\pi]$ because of the periodicity, in order to enhance the visual display.

In Hill (2002), the geometrical space (location $\vec{x}$ in the flow) and the separation space (scales $\vec{r}$) are made independent by considering the midpoint $\vec{X} = \frac{1}{2}\left(\vec{x} + \vec{x^+}\right)$ with $\vec{x^+} = \vec{x} + \vec{r}$. The same idea is applied here to phase-conditioned structure functions for which the phase ϕ is defined as the phase at the midpoint $\phi = \phi(\vec{X})$.

It is instructive to illustrate the phase-variations of the total strain $S_{ij} = \frac{1}{2}\left(\frac{\partial u_i}{\partial x_j} + \frac{\partial u_j}{\partial x_i}\right)$. $\overline{S}_{ij}$ is the the mean strain rate, viz.

$$\overline{S}_{ij} = \frac{1}{2}\left(\frac{\partial \overline{U}_i}{\partial x_j} + \frac{\partial \overline{U}_j}{\partial x_i}\right), \tag{3.16}$$

where double indices represent summation and $\tilde{S}_{ij}$ is given by

$$\widetilde{S}_{ij} = \frac{1}{2}\left(\frac{\partial \widetilde{U}_i}{\partial x_j} + \frac{\partial \widetilde{U}_j}{\partial x_i}\right). \tag{3.17}$$

For simplicity, subscripts ij are hereafter removed, hence $\langle S\rangle = \langle S_{ij}\rangle$. Therefore, $\langle S\rangle = \overline{S} + \widetilde{S}$ with $\overline{S} = \overline{S_{ij}}$ and $\widetilde{S} = \widetilde{S_{ij}}$. It is important to note here the dependence of $\langle S\rangle$ on the phase ϕ of the coherent motion. This dependence is depicted in Fig. 2 for various values of ϕ/π and y/d, by using experimental data for the CC wake. The maxima of the total strain occur at phases which are $-\pi/2 + 2n\pi$ $(n \in \mathbb{N})$, corresponding to the position of the saddle points. Also illustrated in the same figure are the streamlines of the coherent vortices. The most visible are two of them, rotating clockwise (the upper stream moves from left to right). The centres of these vortices are located at $y/d \approx 1.4$ and phases $\phi = -3\pi/2 \pm 2n\pi$ $(n \in \mathbb{N})$ and correspond to the minimum total strain $\langle S\rangle$.

Phase-averaging inescapably leads to a dependence on the phase ϕ, and eventually on the scale r of the flow, as is the case for structure functions of any order.

In this context, the isotropic relation between second-order structure functions of the longitudinal velocity components and those of the transverse velocity components may be written as

$$\left\langle(\Delta u_\perp)^2\right\rangle_{iso}(r,\phi) = \left(1 + \frac{r}{2}\frac{\partial}{\partial r}\right)\left\langle(\Delta u)^2\right\rangle(r,\phi), \tag{3.18}$$

where the second-order structure function $\left\langle(\Delta u_\perp)^2\right\rangle(r,\phi)$ is the average of the square of the velocity increments conditioned by the phase ϕ of the coherent motion.

Note the analogy between (3.18) and its time-averaged counterpart Eq. (3.1). It is obvious that such a LI criterion at each phase of the motion is much more restrictive

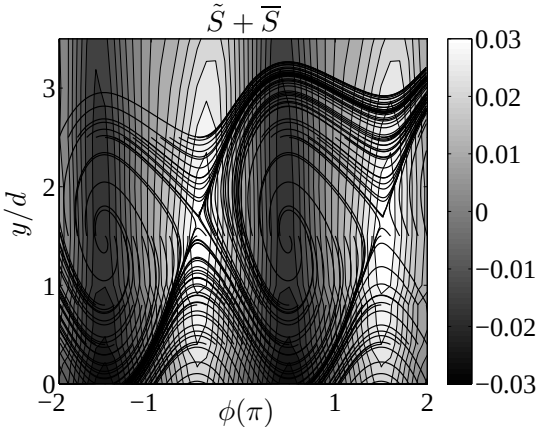

FIGURE 2. The total strain $\langle S \rangle \cdot d/U_0$ as a function of the phase ϕ and the vertical position in the wake, y/d (CC). The solid lines represent the streamlines of coherent vortices.

than its time-averaged counterpart, Eq. (3.1). All the other LI criteria based on time-averaged statistics may be written by using the phase-averages. Henceforth, time averages $\overline{[\cdot]}$ and phase averages $\langle \cdot \rangle$ are used interchangeably.

3.2. *Phenomenological LI tests*

These tests aim at defining LI criteria involving large-scale phenomena, particularly the mean strain $\overline{S}$ as well as $\tilde{S}$. As emphasised earlier, the phase-averaged strain rate $\tilde{S}$ depends on the phase of the coherent motion. We will first consider relatively conventional LI tests involving time averages (Subsection 3.2.1). Time averages will be applied to the absolute value (denoted by $|\cdot|$) of $\langle S \rangle$ because anisotropy is insensitive to the sign of the total strain. Therefore, in the next subsection, the fluctuating strain is implicit in the quantity $\widetilde{S}_t$ defined by

$$\widetilde{S}_t = \overline{|\langle S \rangle|} = \overline{\left|\overline{S} + \tilde{S}\right|}, \tag{3.19}$$

which does not depend on ϕ and is necessarily positive. Note that we have chosen the absolute value as one possible norm, but other definitions may be used instead, such as the maximum value, or L_2 norm.

3.2.1. *Time-averaged quantities*

We examine whether isotropy is valid at a given scale, by using several criteria, adapted to the investigated scales: large, intermediate and viscous. The methodology chosen in order to answer these questions is based on calculating characteristic times

- of the mean and coherent strain time scales. This represented by $\widetilde{S}_t^{\,-1}$ can induce anisotropy.
- of the structures present at any other scale, $\tau(r)$. This scale can be large, in which case large-scale statistics can relate to both turbulent and coherent motions. $\tau(r)$ can also relate to inertial or small-scales, mostly characterized by random fluctuations.

We first investigate the isotropy at large scales, by calculating the ratio of the characteristic time of the coherent strain and that of the total cascade.

The starting point is the study of Durbin & Speziale (1991) for a uniformly sheared flow. In order to study LI, they derived a budget equation for each component of the mean energy dissipation rate, which accounted for the mean strain, $\overline{S}$. They demonstrated that a criterion for LI must be $\overline{S}\overline{q^2}/\overline{\epsilon} \ll 1$, where $\overline{q^2}/\overline{\epsilon}$, the ratio of the total kinetic energy

and the mean energy dissipation rate, is the characteristic time of the (total) cascade. Therefore, Durbin and Speziale's criterion simply signifies that the ratio between the total cascade time and the characteristic time of the strain should be much smaller than 1. We should mention here that, in our opinion, this criterion has more to do with 'isotropy' rather than 'local isotropy', since no particular scale is involved. Antonia & Kim (1994) noted that a disadvantage of using $\overline{S}\overline{q^2}/\overline{\epsilon}$ is that it is zero at the wall (see their Fig. 8) where $\overline{S}$ is largest. Moreover, Gualtieri *et al.* (2002) suggested the same idea in their relation (14) which expresses $\overline{S}\overline{q^2}/\overline{\epsilon}$ as a function of two large scales, hence with no dependence on any small scale. Therefore, this criterion is not useful for testing local isotropy in highly sheared flows, and in particular for the flow under consideration. We will then adapt it to our case, but specifically for investigating local isotropy.

By analogy, we presume that the coherent strain rate $\widetilde{S}$ associated with the organized motion must play an additional role. This can be emphasised by deriving a transport equation for the energy dissipation rate, in which the organized motion is accounted for. We introduce a ratio between the total cascade time $\overline{q^2}/\overline{\epsilon}$ and $1/\widetilde{S}_t$, the inverse of the sum of the mean and of the absolute value of the coherent strain. Following Durbin & Speziale (1991), one can therefore argue that local isotropy should be a plausible hypothesis when the total strain time-scale is very large compared to the total cascade time scale. In other words,

$$\widetilde{S}_t\overline{q^2}/\overline{\epsilon} \ll 1. \tag{3.20}$$

For intermediate scales which may be associated with the RSR, the local isotropy criterion translates to $\tau(r) \ll (\widetilde{S}_t)^{-1}$, or, $\mathcal{R}(r) = \tau(r)\widetilde{S}_t \ll 1$, or the equivalent expression in spectral space, *viz.* $\mathcal{R}(k) = \tau(k)\widetilde{S}_t \ll 1$. In both spaces, different expressions of the energy transfer characteristic time may be used, such as that suggested by Batchelor (1959), Kraichnan (1971) and Danaila & Antonia (2009) in spectral space $\tau(k) = \left(\int_0^k p^2 E(p)dp\right)^{-1/2}$. This characteristic time is dimensionally consistent with that proposed by Onsager (1949) $\tau(k) = \left(k^3 E(k)\right)^{-1/2}$. Injecting a particular expression of the 3D energy spectrum, *e.g.* $E(k) \propto \overline{\epsilon}^{2/3}k^{-5/3}$ in the criterion $\mathcal{R}(k) = (k^3\overline{\epsilon}^{2/3}k^{-5/3})^{-1/2}\widetilde{S}_t$ leads to the determination of a wavenumber k beyond which LI in the IR (or RSR, for finite Reynolds numbers) is an adequate approximation. This wavenumber is given by $k \gg k_{\widetilde{S}} = \sqrt{\widetilde{S}_t^3/\overline{\epsilon}}$.

This result generalises the characteristic strain-rate length-scale proposed by Corrsin (1958), for the purpose of assessing LI in the inertial range, *i.e.*

$$L_{\overline{S}} = \sqrt{\overline{\epsilon}/\overline{S}^3}. \tag{3.21}$$

Obviously, the same methodology can be applied in physical space. In this case, an expression for the characteristic time at an arbitrary scale r has been proposed by Danaila *et al.* (2012).

We briefly recall here Casciola *et al.* (2003)'s corresponding arguments in physical space. In particular, these authors provided a physical interpretation of $L_{\overline{S}}$, emphasising that $L_{\overline{S}}$ represents the cross-over between contributions from the production term due to the mean shear and the non linear transfer term in the spherically averaged scale-by-scale kinetic energy budget. In the presence of an organized motion, the production term at each scale can be defined by (Thiesset *et al.* (2011))

$$\mathcal{P}(r) = 2\overline{\left\langle \Delta u_i' \Delta u_j' \right\rangle \left(\frac{\partial \overline{U}_i}{\partial x_j} + \frac{\partial \widetilde{u}_i}{\partial x_j} \right)}. \tag{3.22}$$

In homogeneous turbulence, the limiting value at the largest scales of (3.22) is twice the production term in the one-point kinetic energy budget (Reynolds & Hussain (1972))

$$\mathcal{P} = \overline{\left\langle u_i' u_j' \right\rangle \left(\frac{\partial \overline{U}_i}{\partial x_j} + \frac{\partial \widetilde{u}_i}{\partial x_j} \right)}. \tag{3.23}$$

By considering classical scaling laws such as $\left\langle \Delta u_i' \Delta u_j' \right\rangle \propto \overline{\epsilon}^{2/3} r^{2/3}$, and $\overline{\Delta u' \Delta q'^2} \propto \overline{\epsilon} r$, a characteristic length scale of the form

$$L_{\widetilde{S}} \propto \sqrt{\overline{\epsilon} / \widetilde{S}_t^3}, \tag{3.24}$$

can be derived. $L_{\widetilde{S}}$ represents the separation at which the kinetic energy production due to the total (both mean and coherent) strain and the non-linear energy transfer are of the same order of magnitude. Therefore, a characteristic length scale related to the total strain is derived and its formulation generalizes the length-scale proposed by Corrsin (1958). Note finally that we have illustrated these arguments by using scaling laws such as '$-5/3$' for spectra or '$2/3$' for structure functions. Finite Reynolds numbers effects and therefore departures from the asymptotic values may be taken into account by simply considering true values (i.e. smaller than the asymptotic value of $2/3$) of the scaling exponents for the structure functions

For the far (smallest scales) dissipative range for which the scales are of the same order of magnitude as the Kolmogorov length scale, the associated characteristic time scale is the Kolmogorov time scale $(\nu/\overline{\epsilon})^{1/2}$. When this scale is much smaller than that associated with the total strain $\widetilde{S}_t$, LI is tenable at the level of the Kolmogorov length-scale. Mathematically, this translates to

$$\widetilde{S}_t^{\,*} \equiv (\nu/\overline{\epsilon})^{1/2} \widetilde{S}_t \ll 1, \tag{3.25}$$

where $\widetilde{S}_t^{\,*}$ denotes the Kolmogorov normalised total strain. When this latter criterion is interpreted in the context of length scales, isotropy should apply for length scales much smaller than $L_{\widetilde{S}}^* = \left(\nu \widetilde{S}_t^{-1} \right)^{1/2}$. The same result can be obtained directly in real space, by considering the cross-over between the dissipative term in the scale-by-scale energy budget equation, *viz.* $2\nu \frac{\partial}{\partial r} \overline{\Delta q'^2}$ and the production term (Eq. (3.22)).

3.2.2. *Phase-averaged quantities*

Here, we propose a LI criterion based on the intensity of the turbulent strain at a given scale r. The formulation is the following: "For LI to be valid at a vectorial scale $\vec{r}$, then the intensity of the strain at that scale due to any larger scale must be much larger than the combined effect of the mean shear $\overline{S}$ and of the coherent motion shear, $\widetilde{S}$".

Mathematically, this can be expressed in terms of two inequalities, depending on whether time-averaged quantities are used, viz.

$$s(\vec{r}) \gg \widetilde{S}_t, \tag{3.26}$$

where $s(\vec{r})$ is the time-averaged strain intensity at the scale $\vec{r}$, and

$$s_\phi(\vec{r}, \phi) \gg \widetilde{S}_\phi, \tag{3.27}$$

with

$$\widetilde{S}_\phi = |\langle S \rangle| \,, \tag{3.28}$$

when phase-averaged quantities are used. Here, $s_\phi(\vec{r},\phi)$ is the phase-averaged strain intensity at the scale $\vec{r}$ and the phase ϕ.

The next step is to propose adequate expressions for the turbulent strain intensity $s(\vec{r})$ and $s_\phi(\vec{r},\phi)$. Starting from the definition of the strain tensor $\Sigma = \nabla_{\vec{x}}\vec{u}$, we need to further define the tensor $\mathcal{S}\Sigma$ characterizing the strain at a scale $\vec{r}$ associated with all the larger scales (Mouri & Hori (2010), Danaila *et al.* (2012)), *i.e.* the quantity $\mathcal{S}\Sigma(\vec{r}) \equiv \nabla_{\vec{x}^+}\vec{u}^+ + \nabla_{\vec{x}}\vec{u}$, with $\vec{x}^+ = \vec{x} + \vec{r}$. By considering the two frames to be independent (Monin & Yaglom (2007)), with $\overrightarrow{U}$ identical in the two frames and by invoking the same decomposition as proposed by e.g. Hill (2002) the final result is

$$\mathcal{S}\Sigma(\vec{r}) = \nabla_{\vec{r}}\Delta\vec{u}. \tag{3.29}$$

Therefore, as far as the turbulent field is concerned, the turbulent strain intensity, which is the absolute value of $\mathcal{S}\Sigma$, may be defined as follows

$$s(\vec{r}) = \overline{(\nabla_{\vec{r}}\Delta\vec{u})^2}^{1/2}. \tag{3.30}$$

After some calculations and by supposing that $\overline{\Delta u_j \frac{\partial^2}{\partial r_k^2}\Delta u_j} \approx 0$ (which is strictly true for $\vec{r} \to 0$), the final expression of $s(\vec{r})$ for general turbulent flows in which time-averages are adequate

$$s(\vec{r}) = \left(\frac{1}{2}\mathcal{L}\overline{(\Delta u_i)^2}\right)^{1/2}(\vec{r}), \tag{3.31}$$

where repeated indices indicate summation and $\mathcal{L}$ represents the Laplacian operator. In flows populated by CM, in which phase-averages are more useful, the intensity of the strain depends on both $\vec{r}$ and the phase ϕ, and it reads

$$s_\phi(\vec{r},\phi) = \left(\frac{1}{2}\mathcal{L}\left\langle(\Delta u_i)^2\right\rangle\right)^{1/2}(\vec{r},\phi). \tag{3.32}$$

Calculating the Laplacian of these functions requires estimates of the velocity field in several planes, such as provided by PIV (Particle Image Velocimetry), or, preferably, numerical simulations.

It is important to note that, for LI, the Laplacian can be expressed in spherical coordinates as follows

$$s_\phi(r,\phi) = \left(\frac{1}{r}\frac{\partial}{\partial r}\left\langle(\Delta u_i)^2\right\rangle + \frac{1}{2}\frac{\partial^2}{\partial r^2}\left\langle(\Delta u_i)^2\right\rangle\right)^{1/2}(r,\phi). \tag{3.33}$$

The first term on the right side of Eq. (3.33) has already been proposed by Danaila *et al.* (2012). This expression will be used later in this paper in order to infer s_ϕ and investigate phenomenological LI tests involving phase averages.

4. Results at the centerline of the wake of different obstacles

4.1. *Kinematic LI tests*

4.1.1. *Time-averaged quantities*

Figures 3(a) and 3(b) represent the ratios between calculated and measured second-order structure functions for v and w respectively. For each initial condition, this ratio is almost independent of the Reynolds number (also noted by AZR). The departure from LI

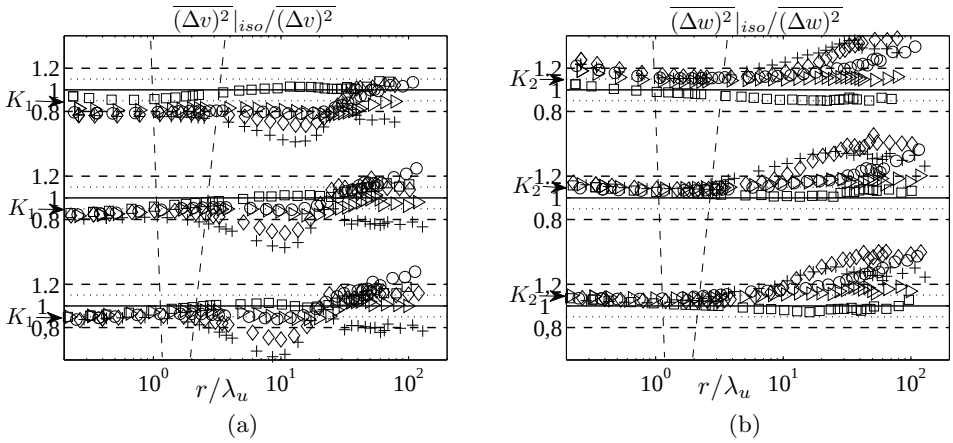

FIGURE 3. (a), (b). Ratios between the isotropic predictions and measured second-order structure functions. In each figure, the increasing Reynolds number is displayed from bottom to top. (a) $\overline{(\Delta v)^2}|_{iso}/\overline{(\Delta v)^2}$. (b) $\overline{(\Delta w)^2}|_{iso}/\overline{(\Delta w)^2}$. ○ CC, □ SqC, ◇ ScC, ▷ P, + SS. —— represents the isotropic ratio of 1, ····· and - - - - represent a departure of 10 and 20% respectively from the isotropic value of 1. Vertical broken lines correspond approximately to the lower and upper limits of the RSR; they diverge upwards as the Reynolds number increases, reflecting the increase in the extent of the RSR with the Reynolds number.

appears to be reasonable in the RSR (with an amplitude of about 10 -15 %) and increases as r decreases through the dissipative range. Note however that for small scales, this ratio is calculated by dividing by small values of second-order structure functions, which may be a possible source of error. Note also that $\overline{(\Delta v)^2} > \overline{(\Delta v)^2}|_{iso}$ and $\overline{(\Delta w)^2} < \overline{(\Delta w)^2}|_{iso}$ for most of the separations.

For larger separations, the departure from LI is maximum at $r \approx 8-10\lambda_u$ and is more noticeable on v than w. At this particular separation, the SS wake exhibits the largest departure from LI followed by the ScC, CC, P and finally the SqC wake for which LI holds for scales as large as 20-30 λ_u. The scale at which the departure from LI is maximum may be associated with the scale at which energy is injected. Therefore, whereas the dissipative scales exhibit a quasi-universal behaviour, the largest scales clearly vary from wake to wake, reflecting the influence of the large-scale organisation on the type of wake generator.

The small-scale limits of the quantities represented in Fig. 3 merit some consideration. As shown by Eq. (3.8), these small-scale limits should be equal to K_1 and K_2 respectively. In order to check the validity of our results for the smallest scales, we have inferred separately K_1, K_2. Several values of K_1 and K_2 in turbulent shear flows are summarized in Browne *et al.* (1987) whereas Antonia *et al.* (1998) reported some of these values in grid turbulence. For all these flows, some departures from LI are discernible, indicating persisting effects of a large scale anisotropic forcing. As pointed out by Antonia *et al.* (1986), the controversy concerning the validity of LI at the level of the dissipative range depends on the severity of the tests themselves and has, to large extent, reflected the difficulties of measuring small scale quantities. Indeed, the imperfect spatial resolution of most hot wire probes, leads to an attenuation of the velocity derivatives. Hence, assessing LI from small scale measurements requires special vigilance.

The correction procedure (2.1) is based on LI whereas the present study aims at testing its validity. We thus need to verify whether the correction induces a bias in the assessment of LI. To this end, we compare the raw and corrected values of the ratios K_1 and K_2.

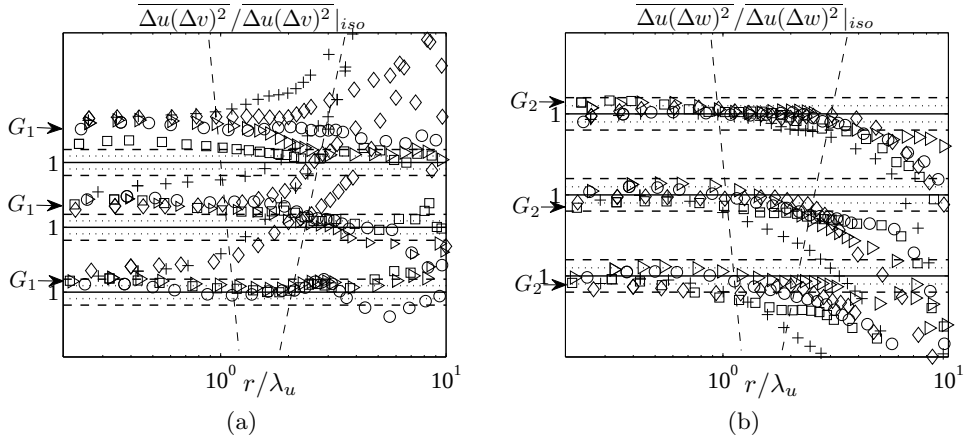

FIGURE 4. (a), (b). Ratio between measured and calculated third-order structure functions. The Reynolds number increases from bottom to top. (a) $\overline{\Delta u(\Delta v)^2}/\overline{\Delta u(\Delta v)^2}|_{iso}$. (b) $\overline{\Delta u(\Delta w)^2}/\overline{\Delta u(\Delta w)^2}|_{iso}$. ○ CC, □ SqC, ♢ ScC, ▷ P, + SS. —— represents the isotropic ratio of 1, ····· and - - - - represent a departure of 10 and 20% respectively from isotropy. The inclined broken lines delineate approximately the boundaries of the RSR.

The corrected values of K_1 and K_2 are calculated by integrating (from 0 to infinity) the corresponding 'true' spectra, *i.e.* obtained from the measured spectra by using Eqs. (2.1) and (2.2). With respect to Eq. (2.2), the values of K_1 and K_2 are modified only slightly by the correction method. The results do not change significantly with the Reynolds number and the type of generator. We have checked that the values of K_1 and K_2 (either corrected, or not) are recovered at the smallest scales of Figs. 3(a) and 3(b) (these are indicated by the horizontal arrows on the left vertical axis of these two figures), in conformity with Eqs. (3.8), thus validating once again the calculated values of the derivative statistics.

Ratios between measured and calculated third-order structure functions are plotted in Fig. 4. In contrast with the second-order structure functions for which the ratio $\overline{(\Delta u_\perp)^2}|_{iso}/\overline{(\Delta u_\perp)^2}$ was displayed, here we represent $\overline{\Delta u(\Delta u_\perp)^2}/\overline{\Delta u(\Delta u_\perp)^2}|_{iso}$.

The departure from the isotropic prediction is approximatively constant (and sufficiently small) within the dissipative range. Moreover, the factors G_1 and G_2 are explicitly recovered in the limit of small separations, indicated by horizontal arrows in Fig. 4.

A strong departure, again more noticeable on v than w, is observed for scales situated within the RSR. For larger separations, the deviation is much bigger than that reported for second-order structure functions, and it continuously grows as the scale keeps increasing. For that reason, values beyond $r = 10\lambda_u$ are not shown. The departure is largest for the SS wake and smaller in order of importance for the ScC, CC, P, and the SqC wakes. Differences between the behaviours of v and w, irrespectively of the criterion, are attributable to the different way energy is injected in the system: here, fluctuations of v are mostly created through instabilities associated with the CM. Further downstream, pressure-velocity correlations act to redistribute the energy, which is continuously reinjected in v by the persistent coherent motion, to the other velocity components. Therefore, a detailed investigation of statistics associated with each individual velocity component may *a priori* highlight energy exchanges among different velocity components and hence possible imbalances between them.

Whereas the evaluation of statistics associated with individual velocity components

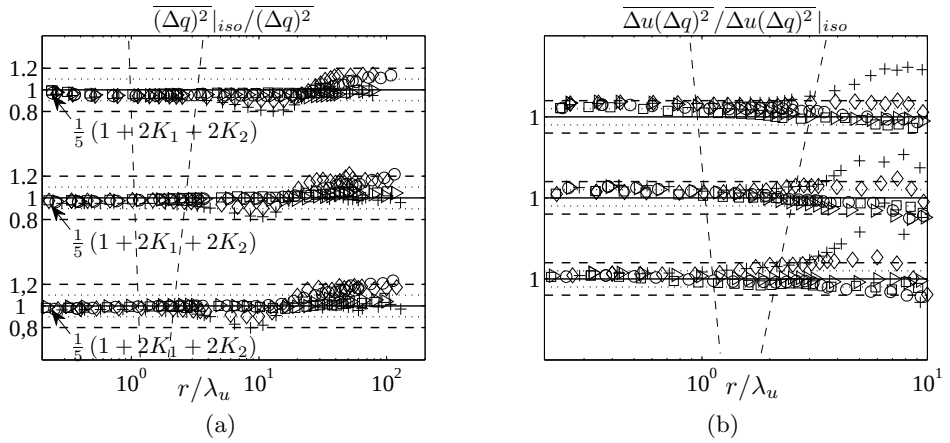

FIGURE 5. (a) Ratio between calculated and measured second order structure functions $\overline{(\Delta q)^2}|_{iso}/\overline{(\Delta q)^2}$. Increasing Reynolds number is displayed from bottom to top. (b) Ratio between measured and calculated third order structure functions $\overline{\Delta u(\Delta q)^2}/\overline{\Delta u(\Delta q)^2}|_{iso}$. Increasing Reynolds number from bottom to top. ○ CC, □ SqC, ◇ ScC, ▷ P, + SS. —— represents the isotropic ratio of 1, ····· and - - - - represent a departure of 10 and 20% respectively from isotropy. The inclined broken lines delineate the approximate boundaries of the RSR.

may result in very tough LI tests due to the previously mentioned imbalances, we continue our investigation by examining the transport of the total kinetic energy at a given scale. Figure 5 represents the isotropic expressions relating second- and third-order structure functions applied to the scalar quantity $\overline{\Delta q^2}$ and its non linear transfer $\overline{\Delta u(\Delta q)^2}$. It is noteworthy that the departure from LI, typically less than 5%, is smaller than that of the individual velocity components v or w. This underlines the compensation which arises from the inequalities $\overline{\Delta v^2} > \overline{\Delta v^2}|_{iso}$ and $\overline{\Delta w^2} < \overline{\Delta w^2}|_{iso}$. In the limit of small separations (Eq. 3.9), $\frac{1}{5}(1+2K_1+2K_2) \to 1$ whereas $K_1 \neq K_2 \neq 1$. Deviations from LI are maximum at $r \approx 10\lambda_u$ for both $\overline{(\Delta q)^2}$ and $\overline{\Delta u(\Delta q)^2}$, as is the case for $\overline{(\Delta v)^2}$ and $\overline{(\Delta w)^2}$. Moreover, the SS wake exhibits once again the strongest anisotropy followed by ScC, CC, P and SqC.

We conclude this temporal-average analysis by summarising the main results obtained by applying several tests of isotropy to second and third-order moments of velocity increments:

- for the smallest scales, *i.e.* in the dissipative range (scales smaller than the Taylor microscale), LI is a good assumption on the wake centerline. For these scales, there is no clear dependence on initial conditions or on the Reynolds number.
- For scales situated in a range loosely identified with the RSR, LI is a reasonable approximation, although there is some dependence on initial conditions and a slight dependence on the Reynolds number. This result holds for tests based on second-order structure functions, whereas third-order structure functions are more severe LI tests (for these tests, the departure from LI is as large as 50%). This is consistent with the analysis of Shen & Warhaft (2000) who showed that anisotropy becomes more and more perceptible with increasing order of the LI test. We infer that for the majority of the LI tests discussed here, LI is tenable for scales smaller than L_a (or 'anisotropy' scale), which lies between 2 and 10 Taylor microscales, depending mainly on the particular test that is used and the Reynolds number and the type of generator.
- Departures from LI are noted for scales larger than L_a, mainly for the transverse

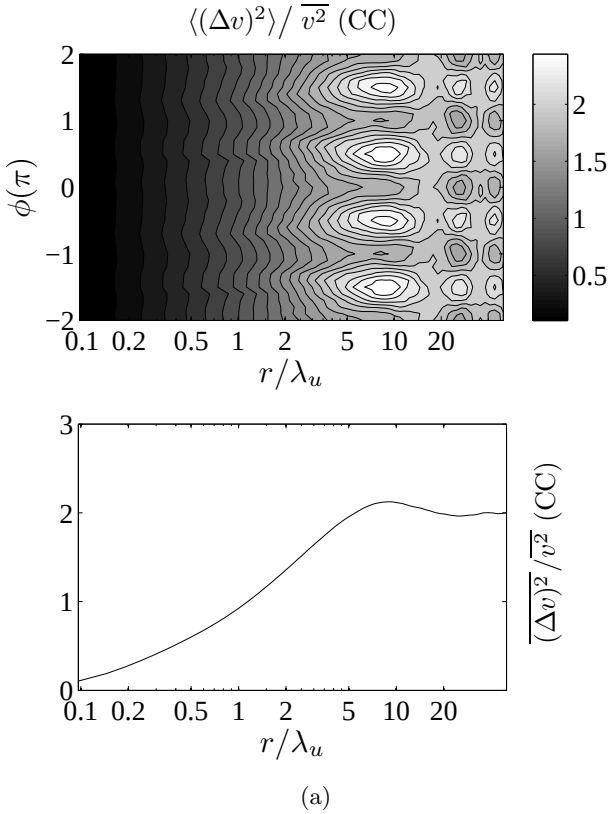

(a)

FIGURE 6. $\langle(\Delta v)^2\rangle(r,\phi)/\overline{v^2}$ (top) and the time-averaged second-order structure function of v (CC), $\overline{(\Delta v)^2}(r)/\overline{v^2}$ (CC). Tha value of the Reynolds number is $R_{\lambda_u} = 190$.

velocity fluctuation v. The observed departures from LI at scales larger than L_a must be correlated with the persisting footprint of the organised motion on v (*e.g.* Hayakawa & Hussain (1989), Matsumura & Antonia (1993)).

We have thus shown that LI is a reasonable approximation for the smallest scales, and is most closely satisfied by the square cylinder wake. The least isotropic wake is that generated by the screen strip, for which vortex merging leads to the production of a very persistent coherent motion. For scales smaller than L_a, which satisfy LI reasonably, there is no perceptible dependence on the Reynolds number, at least for this range of Reynolds numbers.

4.1.2. *Phase-averaged quantities*

Whereas the value of the scale L_a for which LI is no longer valid has been determined from time-averaged quantities, it is worth extending our analysis by examining the dynamical variation of this scale as a function of the phase of the CM.

It is first useful to detail the scale-phase variation of $\langle(\Delta v)^2\rangle(r,\phi)$. Figure 6, top, displays $\langle(\Delta v)^2\rangle(r,\phi)/\overline{v^2}$, as a function of the scale r normalised by the Taylor microscale λ_u and the phase ϕ (normalised by π). Note that in homogeneous turbulence, this normalised ratio should be equal to 2 at large scales. The values of the phase conditioned second-order structure functions progressively increase as r keeps increasing, and reach a maximum for $r/\lambda_u \approx 9$ (this scale is equal to half the distance between two successive

vortices), followed first by a slight decrease and then by a quasi-periodic behaviour for the largest scales. The maxima of $\langle(\Delta v)^2\rangle(r,\phi)/\overline{v^2}$ occur at scales which are multiples of the first maximum. The trend of $\langle(\Delta v)^2\rangle(r,\phi)/\overline{v^2}$ is uniform in ϕ for small scales, consistent with the fact that small-scale fluctuations are not dynamically connected with the CM. At larger scales, where the CM is present, there is a hint of periodicity along the ϕ axis (for $r/\lambda_u \approx 2$), followed by a clear periodicity at scales $r/\lambda_u \approx 9$, as emphasised earlier. At these scales, the energy distribution is strongly affected by the presence of the CM. The average along the ϕ axis of the function $\langle(\Delta v)^2\rangle(r,\phi)/\overline{v^2}$ is equal to $\overline{(\Delta v)^2}(r)/\overline{v^2}$, as shown in Fig. 6 (bottom) as a function of r/λ_u. Similarly to the large-scale periodic trend of the scale-phase second order structure functions, the large-scale limit of $\overline{(\Delta v)^2}(r)/\overline{v^2}$ overshoots the value of 2 at $r/\lambda_u \approx 9$, then decreases and finally tends towards a constant for larger scales.

The dynamical aspect of $\langle(\Delta v)^2\rangle(r,\phi)$ should be understood in association with the phase variations of the total strain (Fig. 2). In particular, for $y = 0$ for which the results in Fig. 6 were obtained, we note that the maxima of $\langle(\Delta v)^2\rangle(r,\phi)$ correspond to the phases of the CM where the strain is extremum (either positive, or negative).

We now present results for one LI test from a dynamical viewpoint, i.e. the ratio between $\left\langle(\Delta u_\perp)^2\right\rangle_{iso}(r,\phi)/\left\langle(\Delta u_\perp)^2\right\rangle(r,\phi)$, where $\left\langle(\Delta u_\perp)^2\right\rangle_{iso}$ is given by relation (3.18). This ratio is illustrated in Fig. 7 on the wake centerline, for the same Reynolds number ($R_{\lambda_u} \simeq 190$) and for three obstacles only. We have selected the SqC, CC and SS, because they represent the two extrema (the most and least isotropic, SqC and SS respectively), as well as an intermediate case, CC, representative of many practical applications. If LI holds at a scale r and a phase ϕ, then the ratio $\left\langle(\Delta u_\perp)^2\right\rangle_{iso}(r,\phi)/\left\langle(\Delta u_\perp)^2\right\rangle(r,\phi)$ should be equal to 1.

For SqC (Fig. 7(a)), the values of $\left\langle(\Delta u_\perp)^2\right\rangle_{iso}(r,\phi)/\left\langle(\Delta u_\perp)^2\right\rangle(r,\phi)$ range between 0.8 and 1.2 (the colorbar of the figure goes down to 0.3 for the sake of uniformity between the three parts of this figure). More Precisely, the values of this ratio are approximately equal to 0.8 for the smallest scales associated with the dissipative range. The departure from isotropy is of the order of 20%, independently of the scale, and is fully consistent with that reported for time-averaged quantities (Fig. 3(a)). These values monotonically increase for the RSR scales (between 1 and 10 λ_u). The isotropic value of 1 is reached for scales approximately equal to 15 λ_u, with very slight variations around this value. Therefore, the dynamical evolution of the scale L_a exhibits smooth variations around the value of $15\lambda_u$. Note that the value of L_a obtained from time-averaged statistics is 20-30 λ_u. This is consistent with the fact that dynamical tests are more restrictive.
The maximum departure of the ratio from the isotropic value of 1 is associated with two kinds of points in Fig. 7(a). First, there are points for which the value of $\left\langle(\Delta u_\perp)^2\right\rangle_{iso}(r,\phi)/\left\langle(\Delta u_\perp)^2\right\rangle(r,\phi)$ is 0.8. This occurs at phases which are odd multiples of $\pi/2$, for which the absolute value of the total strain is maximal, and with scales as large as $\approx 20\lambda_u$. Second, there are locations where $\left\langle(\Delta u_\perp)^2\right\rangle_{iso}(r,\phi)/\left\langle(\Delta u_\perp)^2\right\rangle(r,\phi) \approx 1.2$ (the maximum positive departure from 1). These points are situated at scales as large as 30 λ_u and at phases corresponding to integer multiples of π, for which the large-scale strain is *a priori* absent.

For CC, LI is tenable up to scales approximately equal to $10\lambda_u$. This limit is larger for phases where the coherent strain is absent and smaller when the coherent strain is important (either positive, or negative). The value of L_a inferred from time-averaged statistics (Fig. 3.1) is 15 λ_u. The maximum departure from LI occurs at $r \approx 15\lambda_u$ (smaller than that for the SqC) and for phases corresponding to the coherent strain extrema. Finally, for SS, the values of the ratio $\left\langle(\Delta u_\perp)^2\right\rangle_{iso}(r,\phi)/\left\langle(\Delta u_\perp)^2\right\rangle(r,\phi)$ are

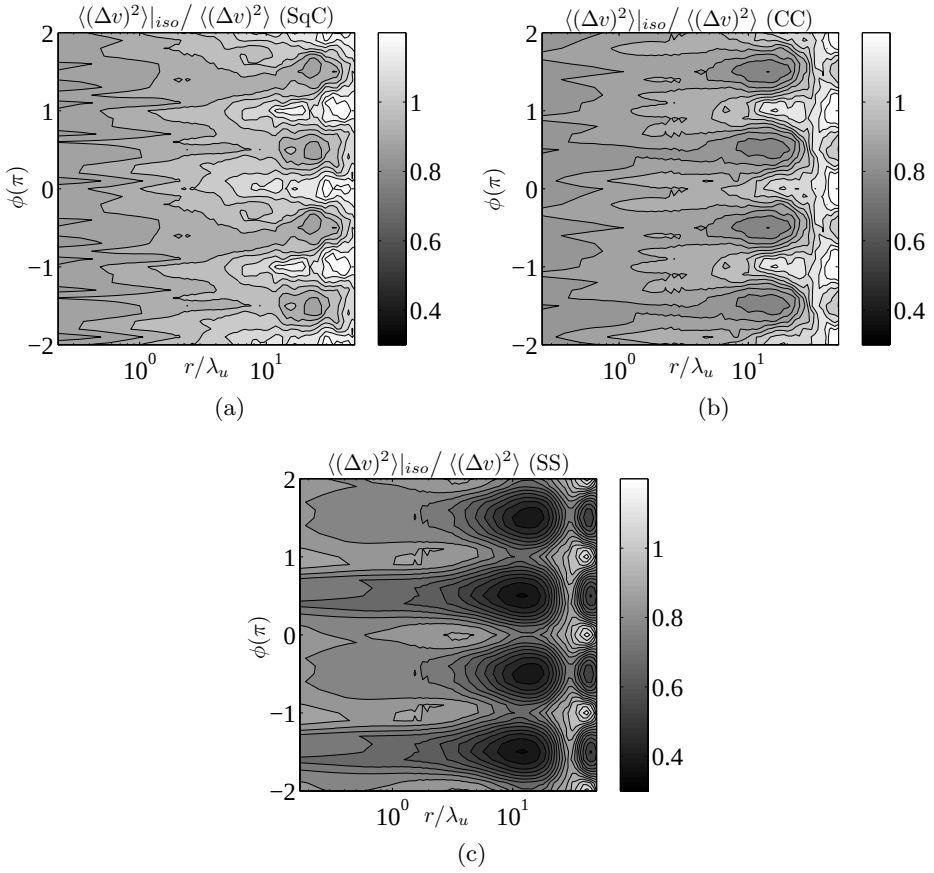

FIGURE 7. The dependence of $\langle(\Delta u_\perp)^2\rangle_{iso}(r,\phi)/\langle(\Delta u_\perp)^2\rangle(r,\phi)$ on r/λ_u and $\phi(\pi)$. (a) SqC. (b) CC. (c) SS. The value of $R_{\lambda_u} \simeq 190$, closely the same for the three obstacles.

as small as 0.4, thus exhibiting the largest anisotropies. The dynamical behaviour of L_a reveals variations between $2\lambda_u$ and 20 λ_u. The minima are associated with phases equal to odd multiples of $\pi/2$ (where the absolute value of the coherent strain is maximum), whereas the maxima correspond with phases where the coherent motion strength is zero. The value of L_a obtained from time-averaging is approximately $10\lambda_u$, which is again larger than that determined through the more refined and stringent dynamical tests. The largest anisotropy occurs at $r \approx 10\lambda_u$ and for phases for which the strength of the coherent strain is the largest.

4.2. *Phenomenological LI tests*

A direct connection has been established between the large-scale strain and anisotropy. We now aim at quantifying explicitly the effect of the strain on LI.

Time-average quantities are first examined in 4.2.1. Phase-averaged quantities are considered in 4.2.2.

4.2.1. *Time-averaged quantities*

We now present experimental results obtained in the intermediate field. On the wake centreline, the transverse velocity component v constitutes the most important contribu-

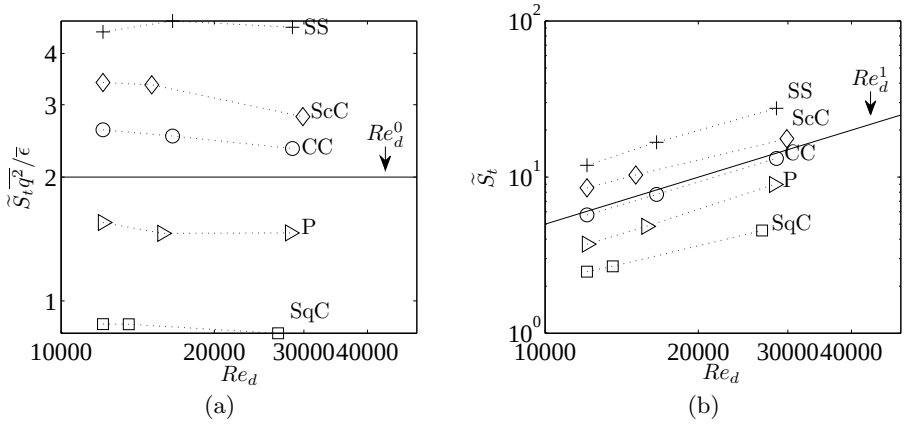

FIGURE 8. (a) $\widetilde{S}_t\overline{q^2}/\overline{\epsilon}$, —— : Re_d^0. (b) Absolute value of the coherent shear $\widetilde{S}_t$ for various Reynolds numbers, —— : Re_d^1. ○ CC, □ SqC, ◇ ScC, ▷ P, + SS.

tion to the rate of coherent strain, *i.e.* $\widetilde{S}_t \approx \overline{\left|\frac{\partial \widetilde{v}}{\partial x}\right|}$ (here, the spatial derivative is calculated from the time/phase derivative via Taylor's hypothesis).

In Fig. 8 (a), we plot the values of $\widetilde{S}_t\overline{q^2}/\overline{\epsilon}$ for each generator. For each wake, the inequality $\widetilde{S}_t\overline{q^2}/\overline{\epsilon} \ll 1$ is violated, which is consistent with the persistence of large-scale anisotropy. SS is most influenced by the rate of coherent strain with $\widetilde{S}_t\overline{q^2}/\overline{\epsilon} \approx 4.5$ followed by ScC ($\widetilde{S}_t\overline{q^2}/\overline{\epsilon} \approx 3.2$), CC ($\widetilde{S}_t\overline{q^2}/\overline{\epsilon} \approx 2.5$), P ($\widetilde{S}_t\overline{q^2}/\overline{\epsilon} \approx 1.5$) and SqC ($\widetilde{S}_t\overline{q^2}/\overline{\epsilon} \approx 0.9$).

In conclusion, by comparing the characteristic time of the coherent motion strain rate with that associated with the total cascade, we have again confirmed that at the centerline of the wake, where the mean strain rate is equal to zero, global isotropy is unlikely to hold.

We next address the influence of the Reynolds number via dimensional arguments which assume that the most appropriate scales are U_d (the velocity defect) and $y_{0.5}$ (the half-width of the mean velocity profile), even though these similarity scales apply strictly to the far field. Therefore,

$$\begin{aligned} \widetilde{S}_t &\propto U_d/y_{0.5}; \\ \overline{q^2} &\propto U_d^2; \\ \overline{\epsilon} &\propto U_d^3/y_{0.5}. \end{aligned} \tag{4.1}$$

Further, by considering that at this location in the flow $U_d \propto U_0$ and $y_{0.5} \propto d$, and provided the proportionality constants do not vary discernibly with the Reynolds number, their ratio leads to

$$\widetilde{S}_t\overline{q^2}/\overline{\epsilon} \propto Re_d^0, \tag{4.2}$$

where Re_d is the Reynolds number based on U_0 and d. This indicates that the ratio $\widetilde{S}_t\overline{q^2}/\overline{\epsilon}$ is constant with respect to Re_d. The coherent shear is expected to affect significantly the turbulent field, independently of the Reynolds number. Both Figs. 8(a) and 8(b) suggest that the dimensional analysis which predicts the evolution of $\widetilde{S}_t\overline{q^2}/\overline{\epsilon}$ and of $\widetilde{S}_t$ with the Reynolds number is well supported by the experimental data. At this stage, it would appear that, in the presence of an anisotropic organised motion, the attainment of an asymptotic isotropic state for large scales and large Reynolds numbers is questionable. This is not surprising.

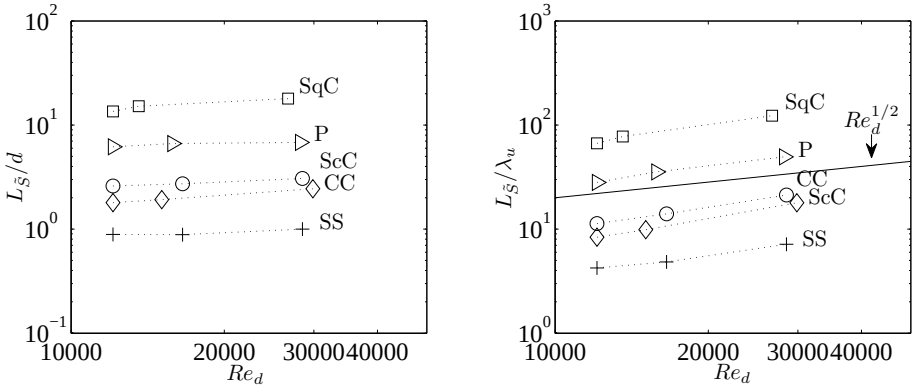

FIGURE 9. (a) Variation of $L_{\widetilde{S}}/d$ with Re_d, (b) Variation of $L_{\widetilde{S}}/\lambda_u$ with Re_d. —— : $Re_d^{1/2}$. ○ CC, □ SqC, ◇ ScC, ▷ P, + SS.

We investigate the possible dependence of the scale $L_{\widetilde{S}}$ on the initial conditions and the Reynolds number based on the upstream mean velocity field. The same dimensional arguments as used previously in this section lead to

$$L_{\widetilde{S}}/d \propto Re_d^0,$$
$$L_{\widetilde{S}}/\lambda_u \propto Re_d^{1/2}. \tag{4.3}$$

The length-scale $L_{\widetilde{S}}$ is therefore constant with respect to the Reynolds number and the ratio between $L_{\widetilde{S}}$ and λ_u increases. We have chosen to study the evolution of $L_{\widetilde{S}}$ with respect to λ_u since λ_u is often identified with the scale at which the non-linear transfer is maximum. Further, λ_u can be determined reasonably accurately.

Experimental data represented in Fig. 9(a) show that the coherent shear length scale $L_{\widetilde{S}}$ increases from $1d$ for SS to $10d$ for SqC. Whilst expressing $L_{\widetilde{S}}$ in terms of d may not be particularly meaningful since d is not a local scale, the fact that the variation of $L_{\widetilde{S}}$ with Re_d is negligible signifies that $L_{\widetilde{S}}$ is a geometrical scale linked to initial conditions through the total strain $\widetilde{S}_t$.

In order to test Eq. (4.3), the ratio $L_{\widetilde{S}}/\lambda_u$ is plotted in Fig. 9(b). The magnitude extends between 4 to $8\lambda_u$ for the SS wake. This value corresponds roughly with the position of the maximum departure from the isotropic value of '1' of the test observed in Fig. 3(a) for instance. $L_{\widetilde{S}}$ also corresponds to the scale at which the departure from LI is first noticeable in Figs. 3(a), 3(b) and 5(a). Therefore, it corresponds to the scale L_a which we wish to quantify phenomenologically. For SqC, the ratio $L_{\widetilde{S}}/\lambda_u$ is about 100, which is consistent with LI for this particular set of initial conditions.

We conclude this subsection by underlining the fact that, on the wake centerline, phenomenological LI tests based on time-averages reinforce the message already delivered via the conventional, kinematic tests. More specifically, i) the large scales are not isotropic; and ii) for the intermediate scales, L_a is as large as 100 λ_u for SqC, $10 \rightarrow 20$ λ_u for CC and 4 to 8 λ_u for the least isotropic flow, viz. SS. Therefore, $L_{\widetilde{S}}$ represents a good approximation to the anisotropy scale L_a, as determined from LI tests involving time-averaged quantities.

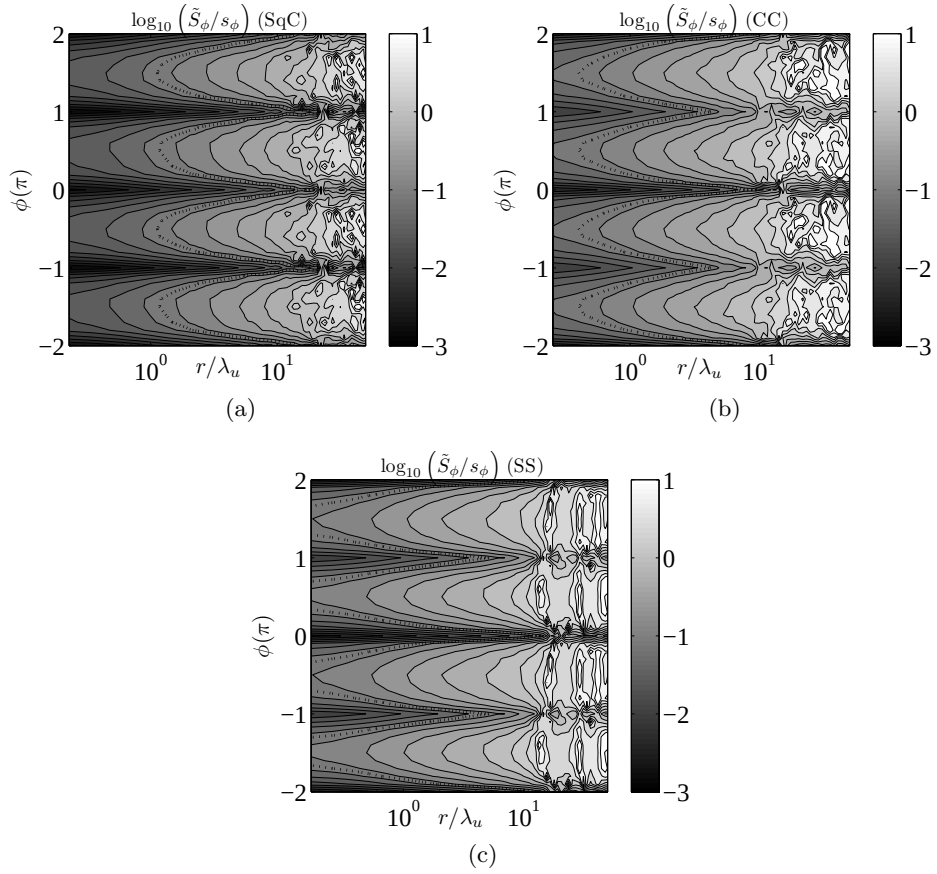

FIGURE 10. Values of $\log_{10}(\tilde{S}_\phi/s_\phi)$ as functions of r/λ_u and the phase ϕ/π. (a), SqC. (b), CC. (c), SS. $R_{\lambda_u} \simeq 190$. The dotted lines represent the scale L_{-1}.

4.2.2. *Phase-averaged quantities*

Here, we test the phenomenological LI criterion $s_\phi(r,\phi) \gg \tilde{S}_\phi(\phi)$ against experimental data. Figure 10 depicts $\log_{10}(\tilde{S}_\phi/s_\phi)$ as a function of r/λ_u and the phase ϕ/π, for three obstacles: SqC (Fig. 10(a)) which has been shown to be the most isotropic flow, followed by CC (Fig. 10(b)) and SS (Fig. 10(c)), the least isotropic wake. The LI criterion may be expressed as follows: 'LI should hold if $\log_{10}(\tilde{S}_\phi/s_\phi) \leq -1$'.

For the three figures, small values of $\log_{10}(\tilde{S}_\phi/s_\phi)$ (dark zones) occur for small scales, whereas large values (much larger than -1), as highlighted by white regions, are found mostly at large scales. The curve for which $\log_{10}(\tilde{S}_\phi/s_\phi) = -1$, called '$L_{-1}$', is represented by dotted lines on the three figures. This curve separates the region of small values of r (for which LI holds), from the region of large scales, the latter being anisotropic. The scale L_{-1} obviously depends on ϕ. Its magnitude varies between 1 and $20\lambda_u$ for SqC, 0.5 and 10 λ_u for CC and 0 and $8\lambda_u$ for SS. The phase for which L_{-1} is minimum is fully correlated with the extremum values of the coherent strain $\tilde{S}_\phi$ (Fig. 2). At the phases for which $\tilde{S}_\phi = 0$, the influence of the coherent motion is absent, so that LI is free to develop and L_{-1} can increase. Temporal averages of $L_{-1}(\phi)$ are fully consistent with different estimations of the anisotropy scale L_a, as discussed previously. Note however that the

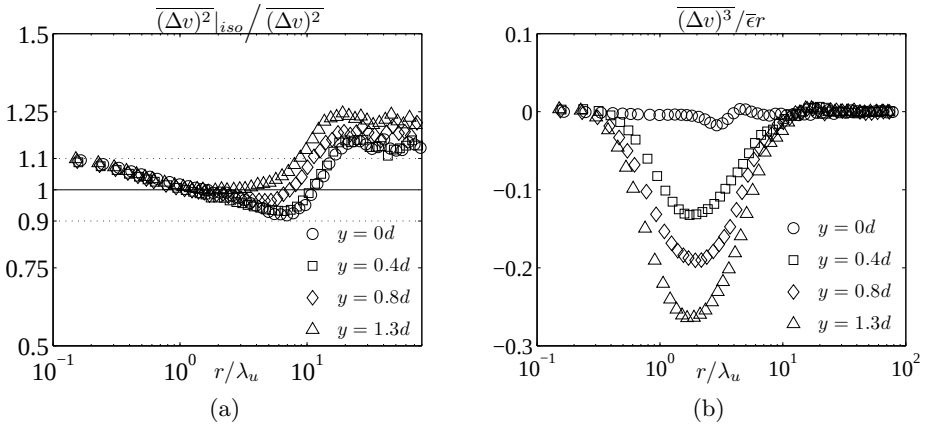

FIGURE 11. Values of the ratios (a): $\overline{(\Delta v)^2}_{iso}/\overline{(\Delta v)^2}$ and (b): $\overline{(\Delta v)^3}/\bar{\epsilon}r$, at several distances away from the CC wake centerline as functions of r/λ_u, at $R_{\lambda_u} \simeq 70$. $\circ$, $y/d = 0$; $\square$, $y/d = 0.4$; $\Diamond$, $y/d = 0.8$; $\triangledown$, $y/d = 1.3$. In (a), the horizontal dotted lines delineate the boundaries of $\pm 20\%$ departures from the isotropic value of 1.

scale L_{-1}, through its dependence on the phase, provides more insight into the dynamics of the flow.

5. Results in presence of a mean shear

We now focus on the sheared region of the flow where the mean shear is not negligible. For simplicity, LI is tested only for CC, at several locations away from the axis, up to $1.3d$. This distance corresponds to a maximum absolute value of the mean shear. The presentation of the results is organised in similar manner to that for the wake centerline. Subsection 5.1 deals with kinematic LI tests, whereas phenomenological tests are discussed in Subsection 5.2. In each subsection, both time-averaged and phase-averaged quantities are used.

5.1. *Kinematic LI tests*

5.1.1. *Time-averaged quantities*

Figure 11(a) represents the ratio between the isotropic estimate of the second-order structure functions of the vertical velocity fluctuations $\overline{(\Delta v)^2}_{iso}$ (as given by relation 3.1) and the measured value of $\overline{(\Delta v)^2}$, as a function of the normalized scale r/λ_u and for several distances from the wake centerline. For isotropy, this ratio should be equal to 1, independently of the scale. At the wake centerline ($y/d = 0$), $\overline{(\Delta v)^2}_{iso}/\overline{(\Delta v)^2}$ is very close to 1 for scales in the range $1 \to 3\lambda_u$, which corresponds approximately to the RSR. For larger scales, this ratio diminishes to values as small as 0.8, followed by a rapid tendency towards a plateau, with a magnitude of about 1.25 at scales equal to or larger than $20\lambda_u$.

At a small distance from the wake centerline ($y/d = 0.4$), the results follow closely those at the centerline. Further away, at $y/d = 0.8$, the extent to which LI holds is comparable to that at the centerline. The scales for which the ratio $\overline{(\Delta v)^2}_{iso}/\overline{(\Delta v)^2} \approx 1$ are almost the same as those for $y/d = 0$, whereas for larger scales the departure from 1 is greater (~ 1.3). Finally, at $y/d = 1.3$, the large-scale anisotropy is significant, arguably because the effect of the shear is more persistent. The ratio $\overline{(\Delta v)^2}_{iso}/\overline{(\Delta v)^2}$ is as large as 1.4 at the largest scales. Noticeable is the fact that, for all locations, LI holds well within

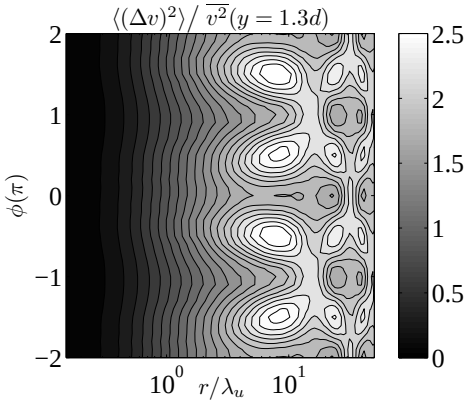

FIGURE 12. Values of $\langle(\Delta v)^2\rangle(r,\phi)/\overline{v^2}$ as a function of r/λ_u and the phase $\phi(\pi)$ at $y = 1.3d$ and $R_{\lambda_u} \simeq 70$.

the RSR, whereas the small departure from isotropy (up to 10%) appears to be more important in the dissipative range. The latter result is very likely caused by dividing by small values of $\overline{(\Delta v)^2}$.

Figure 11(b) illustrates the third-order structure function of the vertical velocity component v, normalised by $\bar{\epsilon}r$ for the four spatial locations investigated. At the wake centerline, this ratio is very nearly equal to zero throughout the whole range of scales, as expected from symmetry. With increasing distance from the centerline, this dissymmetry coefficient progressively decreases for scales associated with the RSR, down to values as low as -0.25. For the largest scales, this coefficient is again very nearly equal to zero. Hence, the inconsistency between Figs. 11(a) (which is rather a proof of LI) and 11(b) hinges on the fact that $\langle(\Delta v)^3\rangle$ is a test of symmetry rather than a LI test. In addition, it is interesting to note that the behaviour of $\overline{(\Delta v)^3}$ appears to be intimately connected to the mean shear $\overline{S}$. Indeed, the sign of $\overline{(\Delta v)^3}$ is opposite to that of $\overline{S}$ and its maximum value reflects the magnitude of the mean shear. Although not shown here for y larger than $1.3d$ (maximum shear), $\overline{(\Delta v)^3}$ begins to decrease towards zero. Further analysis is needed to derive a relation between $\overline{(\Delta v)^3}$ and $\overline{S}$

In summary, away from the centerline, anisotropy is unambiguously present at the largest scales of the flow. There is no strong evidence of anisotropy at scales associated with the RSR. However, it is not possible to draw firm conclusions on whether departures from local isotropy in the dissipative range are genuine or simply an artefact of dividing by small quantities.

5.1.2. *Phase-averaged quantities*

We next turn our attention to kinematic LI tests applied to phase-averaged quantities. These are presented for the vertical component of the velocity field, v.

Figure 12 represents the phase-averaged second-order structure functions for v normalized by its variance, $\langle(\Delta v)^2\rangle/\overline{v^2}$, as a function of the scale r/λ_u and the phase $\phi(\pi)$ of the coherent motion, at $y/d = 1.3$. The behaviour of $\langle(\Delta v)^2\rangle/\overline{v^2}$ at $y/d = 1.3$ is very similar to that on the wake centerline.

The dynamical aspect of $\langle(\Delta v)^2\rangle(r,\phi)$ should be understood in association with the phase variations of the total strain, Fig. 2. Careful inspection of this figure reveals that the extrema of the total strain $\overline{S} + \widetilde{S}$ occur at the same phases (i.e. odd multiples of $\pi/2$) almost independently of the spatial location y. A further comment is in order, concerning the regions for which the normalized second-order structure functions of v are maximum.

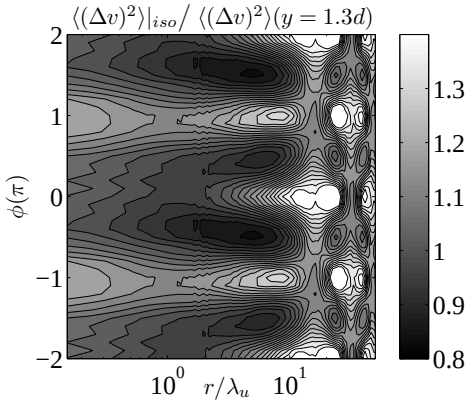

FIGURE 13. The dependence of $\left\langle(\Delta v)^2\right\rangle_{iso}(r,\phi)/\left\langle(\Delta v)^2\right\rangle(r,\phi)$ on r/λ_u and $\phi(\pi)$ at $y/d=1.3$ and $R_{\lambda_u}\simeq 70$.

It has been previously noted (Fig. 6) that these maxima occur at phases for which $\widetilde{S}$ is extremum, and for $r/\lambda_u\approx 9$. It is worth noting that away from the centerline, the periodicity of these regions is not π, but rather 2π (a complete period of the coherent motion). This behaviour is associated with the fact that for e.g. $\phi(\pi)=0.5$, $\widetilde{S}<0$ (see Fig. 2), the total strain $\overline{S}+\widetilde{S}$ is smaller than $\overline{S}$, and for these phases, the local strain is diminished. On the contrary, at $\phi(\pi)=-0.5$ (and multiples), $\widetilde{S}>0$ (see Fig. 2), the total strain $\overline{S}+\widetilde{S}$ is larger than $\overline{S}$, and at these phase locations, the local strain is enhanced. Therefore, the period of any phase-averaged quantity in the sheared region of the wake is exactly 2π. Only at the wake centerline, where $\overline{S}=0$, the period may be π, as emphasised in Fig. 6(a). For phases associated with $\widetilde{S}>0$, therefore with a maximal total strain, the increase of the ratio $\left\langle(\Delta v)^2\right\rangle(r,\phi)/\overline{v}^2$ towards the maximum value of 2.5 is more important and starts at smaller scales ($r/\lambda_u\approx 3$) than for phases where $\widetilde{S}<0$.

We now present results for one LI test from a dynamical viewpoint, i.e. the ratio $\left\langle(\Delta v)^2\right\rangle_{iso}/\left\langle(\Delta v)^2\right\rangle$, where $\left\langle(\Delta v)^2\right\rangle$ is given by relation 3.18. This ratio is illustrated in Fig. 13 at $y/d=1.3$. If LI holds at a scale r and a phase ϕ, then the ratio $\left\langle(\Delta v)^2\right\rangle_{iso}/\left\langle(\Delta v)^2\right\rangle$ should be equal to 1. The maximum departure of the ratio from the isotropic value of 1 is associated with phases which are odd multiples of $\pi/2$, for which the absolute value of the total strain is maximal, and with scales as large as $\approx 20\lambda_u$. At these scales, the value of $\left\langle(\Delta v)^2\right\rangle_{iso}/\left\langle(\Delta v)^2\right\rangle$ is 1.3. The approximate value of the anisotropy scale L_a for the CC wake at $y=1.3d$ is 3 λ_u.

5.2. *Phenomenological LI tests*

The phenomenological LI criterion $s_\phi(r,\phi)\gg\tilde{S}_\phi(\phi)$ is now tested against experimental data. Figure 14 depicts $\log_{10}(\tilde{S}_\phi/s_\phi)$ as functions of r/λ_u and the phase ϕ/π, for the CC wake, at a spatial location $y/d=1.3$ away from the centerline. Again, a possible statement of the LI criterion is 'LI should hold if $\log_{10}(\tilde{S}_\phi/s_\phi)\leq -1$'. As in the case of results previously presented at the wake centerline, small values of $\log_{10}(\tilde{S}_\phi/s_\phi)$ (dark zones) occur for small scales, whereas large values (much larger than -1), as highlighted by white regions, are found mostly at large scales. The curve for which $\log_{10}(\tilde{S}_\phi/s_\phi)=-1$, i.e. '$L_{-1}$', is represented by dotted lines. This curve separates the region of small values of r (for which LI holds), from the region with large anisotropic scales. As emphasised by this figure, L_{-1} varies between $0.8\lambda_u$ and $8\lambda_u$. Its magnitude is smaller than at the wake centerline, where the mean shear is absent. The phase for which L_{-1} is minimum is fully

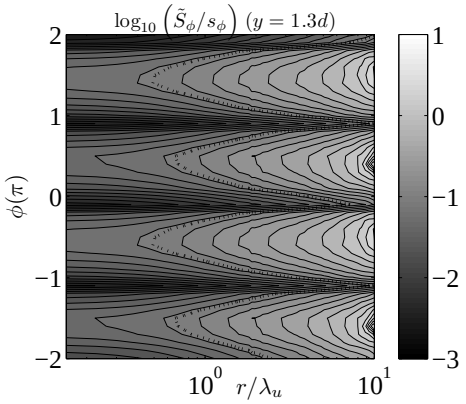

FIGURE 14. Values of $\log_{10}(\tilde{S}_\phi/s_\phi)$ as functions of r/λ_u and the phase ϕ/π, at $y/d = 1.3$. The dotted lines represent the scale L_{-1}.

correlated with the extremum values of the coherent strain $\tilde{S}_\phi$ (Fig. 2). At the phases for which $\tilde{S}_\phi = 0$, the influence of the coherent motion is absent, so that LI becomes more noticeable and L_{-1} can increase.

6. Persisting effects of the coherent motion in the far field

The possibility that the effects of the organized motion or coherent structures persist in the far field is considered here. For this purpose, the downstream evolution of $\widetilde{S}_t\overline{q^2}/\overline{\epsilon}$, $L_{\widetilde{S}}$, $L^*_{\widetilde{S}}$ as well as their ratios need to be examined. It is now well established that the far field of the wake flow is characterised by a self-similar state with respect to the streamwise direction (Townsend (1976), Wygnanski *et al.* (1986), George (1989), Browne & Antonia (1986)) when statistics are normalized by U_d and $y_{0.5}$, as illustrated by relations (4.1).

Furthermore, by using the fact that the downstream evolutions of U_d and $y_{0.5}$ are given by

$$\begin{aligned} U_d &\propto (x - x_0)^{-1/2} \\ y_{0.5} &\propto (x - x_0)^{1/2}, \end{aligned} \tag{6.1}$$

where x_0 is a virtual origin, we expect that

$$\begin{aligned} \widetilde{S}_t\overline{q^2}/\overline{\epsilon} &\propto (x - x_0)^0 \\ \widetilde{S}^* &\propto (x - x_0)^0 \\ L_{\widetilde{S}}/\lambda_u &\propto (x - x_0)^0 \\ L^*_{\widetilde{S}}/\lambda_u &\propto (x - x_0)^0. \end{aligned} \tag{6.2}$$

These relations suggest that $\widetilde{S}_t\overline{q^2}/\overline{\epsilon}$, $L_{\widetilde{S}}$, $L^*_{\widetilde{S}}$ and $\widetilde{S}^*$ do not vary with $x - x_0$.

In the light of these remarks, LI is unlikely to be verified more accurately in the far wake. This would be consistent with the experimental observations of Browne *et al.* (1987), who indicated that anisotropy is not negligible at $420d$. Moreover, our results support the proposition of George (1989) that there is no universal self-similarity (see also Wygnanski *et al.* (1986)) but only local self-similarity conditioned by the topology and amplitude of the organised motion associated with each set of initial conditions. They further strongly point to the likelihood that, associated with the notion of local self-similarity, the level of local anisotropy will differ by varying amounts between far-wakes generated by different obstacles. In particular, the anisotropy in the far-wakes

generated by porous bodies of the type considered in the present study ought to be greater than that in the far-wakes of solid bodies. One cannot rule out that the level of anisotropy may differ among the far-wakes in each of the two previous groups. For example, the far-wake of a solid square cylinder is likely to be be more isotropic than that of a solid circular cylinder.

7. Conclusions and suggestions for future work

The effect on local isotropy due to an anisotropic coherent motion and shear has been assessed by means of hot-wire measurements in two-dimensional wakes downstream of different obstacles.

Isotropy is tested for a wide range of scales, from the dissipative to the largest scales. Different analytical expressions, all based on LI, involving statistics at a particular scale or spatial derivatives, are tested against experimental data. The analytical relations are either kinematic or phenomenological and the LI tests involve either temporal or phase averages, the latter being particularly well suited for characterizing flows populated by coherent motions.

Particular attention has been paid to the centerline of the wake, where we have shown that the largest scales are anisotropic. The assessment of LI was then extended to the inertial and dissipative scales by means of isotropic relations between structure functions. The small scales are not strongly affected by the type of wake-generator. Different isotropy criteria for both dissipative and large scales are recovered by considering the limiting forms of these relations when the separation is either very small or very large. These conclusions seem to point to a 'universal' isotropic behaviour of the small scales. However, in the inertial range, second-order structure functions are closer to isotropy than third-order structure functions, consistent with the conclusions of Shen & Warhaft (2000).

We have shown that isotropy is a reasonable approximation for the smallest scales, especially for the square cylinder. The least isotropic flow is the screen strip wake, for which the merging of vortices arising from Kelvin Helmholtz instabilities is delayed and the CM is more noticeable at $70d$ than for the other wake flows. As far as the influence of the Reynolds number is concerned, we note that over the range of scales for which LI holds, there is no clear dependence on the Reynolds number. LI is tenable for scales smaller than L_a. For scales larger than L_a, departures are clearly visible, especially on the transverse velocity component v.

We have further determined the approximate value of the scale L_a, by using kinematic tests, based on either temporal or phase averages. The largest values of L_a were obtained for SqC, for which the tests involving time-averages led to $L_a \simeq 20 - 30\lambda_u$, whereas the tests based on phase-averages yielded $L_a \simeq 15\lambda_u$ with relatively small variations around this value. Since these latter tests are more stringent, the anisotropy is detected at smaller scales. The smallest values of L_a were provided by SS, for which the tests involving time-averages led to $L_a \simeq 10\lambda_u$, whilst the dynamical tests emphasized that L_a has a maximum value of $20\lambda_u$ (associated with the phases for which the total strain is negligible), and a minimum value as small as $2\lambda_u$ (when the strength of the total strain is most important).

Away from the wake centerline, the value of L_a is small, thus emphasising the effect of the shear which is superposed to that of the coherent motion. Since L_a is not likely to depend on the Reynolds number, it is simply a geometrical scale.

We next addressed the question of correlating the value of L_a with large-scale properties such as the mean strain $\overline{S}$ and the coherent motion strain $\widetilde{S}$, which in turn are linked to the initial conditions (geometrical and hydrodynamical). In the absence of analytical

expressions for L_a, potential surrogates for this scale were identified either from i) time-averaged, or ii) phase-averaged quantities.

i) The first is $L_{\tilde{S}}$, which involves the total strain (the sum of the mean strain and the time-averaged coherent motion strain) and approximates the scale L_a inferred from time-averages reliably.

ii) The second is L_{-1}. To gain some insight into how the organized motion causes departures from isotropy, we have also tested phenomenological criteria for LI using phase-averaged quantities, e.g. the phase averaged strain and phase-averaged structure functions. The scale L_{-1} was constructed so that the intensity of the large-scale strain (including both the mean and coherent motion strain) represents 10% of the small-scale strain. Whereas the threshold of 10% is arbitrarily chosen, we need to recognize that the merit of this phenomenological criterion stands in the fact that it allows LI to be tested at each phase and each scale. The scale L_{-1} involves both the total strain and the turbulent strain intensity at each phase and represents a reasonable surrogate of the scale L_a determined from the phase-averaged quantities. Once again, SqC generates the most isotropic wake, whereas the SS wake is the most anisotropic.

An interesting further perspective of this work would be to establish a $R_{\lambda_u} - \widetilde{S}_t$ phase diagram, thus extending the idea of Schumacher *et al.* (2003) by adding to the mean strain rate the strain rate arising from the coherent motion. This diagram would allow estimates of the combination of R_{λ_u} and $\widetilde{S}_t$ values for which LI is first validated, with the caveat that whilst such estimates may be possible for second and third-order statistics, such as those considered in this paper, they may not exist for higher-order statistics.

The possibility that the effects of the organized motion persist in the the far field has also been addressed. To this end, we have considered some very simple arguments based on self-similarity. We have shown analytically that $\tilde{S}_t\overline{q^2}/\overline{\epsilon}$,$\widetilde{S}^*$, $L_{\tilde{S}}/\lambda_u$ and $L^*_{\tilde{S}}/\lambda_u$ remain constant when the distance downstream of the obstacle increases. The effect of the organized motion is expected to persist even though the distance from the obstacle becomes extremely large. This trend needs to be confirmed by further experiments.

More work is also needed to explain the dynamical processes which result in local anisotropy in the presence of an organized motion, paying particular attention to the influence of the anisotropic energy fluxes. In this context, it would be useful to assess the influence of the coherent motions on scale-by-scale budgets for the energy associated with each velocity component, rather than just the trace $\overline{\Delta q^2}$. This could lead to further insight into the interactions between different velocity components.

Acknowledgement

The financial support of the 'Agence Nationale de la Recherche' (ANR), under the project 'ANISO', is gratefully acknowledged. RAA acknowledges the support of the Australian Research Council. We thank T. Zhou for his contribution to the original experiments carried out, as well as the estimation of the factors K_i.

REFERENCES

Antonia, R.A., Abe, H. & Kawamura, H. 2009 Analogy between velocity and scalar fields in a turbulent channel flow. *J. Fluid Mech.* **628**, 241–268.

Antonia, R.A. & Kim, J. 1994 A numerical study of local isotropy of turbulence. *Phys. Fluids* **6, 2**, 834–841.

Antonia, R. A., Anselmet, F. & Chambers, A. J. 1986 Assessment of local isotropy using measurements in a turbulent plane jet. *J.Fluid Mech.* **163**, 365–391.

Antonia, R. A. & Mi, J. 1998 Approach towards self-preservation of turbulent cylinder and screen wakes. *Exp. Therm. Fluid Science* **17**, 277–284.

Antonia, R. A., Ould-Rouis, M., Anselmet, F. & Zhu, Y. 1997 Analogy between predictions of Kolmogorov and Yaglom. *J. Fluid Mech.* **332**, 395–409.

Antonia, R. A., Zhou, T. & Romano, G. P. 2002 Small-scale turbulence characteristics of two dimensional bluff body wakes. *J.Fluid Mech.* **459**, 67–92.

Antonia, R. A, Zhou, T. & Zhu, Y. 1998 Three-component vorticity measurements in a turbulent grid flow. *J. Fluid Mech.* **374**, 29–57.

Antonia, R. A., Zhu, Y. & Shafi, H. S. 1996 Lateral vorticity measurements in a turbulent wake. *J. Fluid Mech.* **323**, 173–200.

Batchelor, G.K. 1959 Small-scale variation of convected quantities like temperature in turbulent fluid. Part 1. General discussion and the case of small conductivity. *J. Fluid Mech.* **5**, 113–133.

Browne, L. W. B. & Antonia, R. A 1986 Reynolds shear stress and heat flux measurements in a cylinder wake. *Phys. Fluids* **29**, 709–713.

Browne, L. W. B., Antonia, R. A. & Shah, D. A. 1987 Turbulent energy dissipation in a wake. *J. Fluid Mech.* **179**, 307–326.

Cannon, S., Champagne, F. & Glezer, A. 1993 Observations of large-scale structures in wakes behind axisymmetric bodies. *Exp. Fluids* **14**, 447–450.

Casciola, C.M, Gualtieri, P, Benzi, R. & Piva, R. 2003 Scale-by-scale budget and similarity laws for shear turbulence. *J. Fluid Mech.* **476**, 105–114.

Champagne, F. H. 1978 The fine-scale structure of the turbulent velocity field. *J. Fluid Mech.* **86**, 67–108.

Champagne, F. H., Harris, V. G. & Corrsin, S. 1970 Experiments on nearly homogeneous turbulent shear flow. *J. Fluid Mech.* **41**, 81–139.

Cimbala, J.M., Nagib, H.M. & Roshko, A. 1988 Large structure in the far wake of two dimensional bluff bodies. *J. Fluid Mech.* **190**, 265–298.

Corrsin, S. 1958 Local isotropy in turbulent shear flow. *Tech. Rep.*. NACA RM.

Danaila, L., Anselmet, F. & Antonia, R. A. 2001 Turbulent energy scale budget equations in a fully developped chanel flow. *J. Fluid Mech.* **430**, 87–109.

Danaila, L. & Antonia, R. A. 2009 Spectrum of a passive scalar in moderate Reynolds number homogeneous isotropic turbulence. *Phys. Fluids* **21**, 111702–111706.

Danaila, L., Antonia, R. A. & Burattini, P. 2012 Comparison between kinetic energy and passive scalar energy transfer in locally homogeneous isotropic turbulence. *Physica D* **241**, 224–231.

Durbin, P. A. & Speziale, C. G. 1991 Local anisotropy in strained turbulence at high Reynolds numbers. *Journal of Fluids Engineering* **117**, 402–426.

George, W. K. 1989 The self preservation of turbulent flows and its relation to initial conditions and coherent structure. *Advances in Turbulence* .

Gotoh, T., Fukayama, D. & Nakano, T. 2002 Velocity field statistics in homogeneous steady turbulence obtained using a high-resolution direct numerical simulation. *Phys. Fluids* **14**, 1065–1081.

Gualtieri, P., Casciola, C. M., Benzi, R., Amati, G. & Piva, R. 2002 Scaling laws and intermittency in homogeneous shear flow. *Phys. Fluids* **14, 2**, 583–596.

Hayakawa, M. & Hussain, A. K. M. F. 1989 Three-dimensionality of organized structures in a plane turbulent wake. *J. Fluid Mech.* **206**, 375–404.

Hierro, J. & Dopazo, C. 2003 Fourth-order statistical moments of the velocity gradient tensor in homogeneous, isotropic turbulence. *Phys. Fluids* **15**, 3434–3442.

Hill, R.J. 2002 Exact second-order structure-function relationships. *J. Fluid Mech.* **468**, 317–326.

Kang, H. S. & Meneveau, C. 2002 Universality of large eddy simulation model parameters across a turbulent wake behind a heated cylinder. *J. Turbulence* **3**, 1–27.

Kim, J. & Antonia, R. A. 1993 Isotropy of the small scales of turbulence at low Reynolds number. *J. Fluid Mech.* **251**, 219–238.

Kolmogorov, A. 1941 Dissipation of energy in the locally isotropic turbulence. *Dokl. Akad. Nauk. SSSR* **125**, 15–17.

Kraichnan, R. H. 1971 Inertial-range transfer in two-and three-dimensional turbulence. *J. Fluid Mech.* **47**, 525–535.

Krishnamoorthy, L.V. & Antonia, R.A. 1987 Temperature-dissipation measurements in a turbulent boundary layer. *J. Fluid Mech.* **176**, 265–281.

Lavoie, P, Burattini, P., Djenidi, L. & Antonia, R.A 2005 Effect of initial conditions on decaying grid turbulence at low R_λ. *Exp. Fluids* **39**, 865–874.

Matsumura, M. & Antonia, R. A. 1993 Momentum and heat transport in the turbulent intermediate wake of a circular cylinder. *J. Fluid Mech.* **250**, 651–668.

Mestayer, P. 1982 Local isotropy and anisotropy in a high-Reynolds-number turbulent boundary layer. *J. Fluid Mech.* **125**, 475–403.

Monin, A. S. & Yaglom, A. M. 2007 *Statistical Fluid dynamics*, , vol. 2. MIT press.

Morris, S. C. & Foss, J. F. 2005 Vorticity spectra in high Reynolds number anisotropic turbulence. *Phys. Fluids* **17**, 088102.

Mouri, H. & Hori, A. 2010 Two-point velocity average of turbulence: statistics and their implications. *Phys. Fluids* **22**, 115110.

O'Neil, J. & Meneveau, C. 1997 Subgrid-scale stresses and their modelling in a turbulent plane wake. *J. Fluid Mech.* **349**, 253–293.

Onsager, L. 1949 Statistical hydrodynamics. *Nuovo Cimento* **6**, 279–287.

Ould-Rouis, M., Antonia, R. A, Zhou, Y. & Anselmet, F. 1996 Turbulent pressure structure function. *Phys. Rev. Lett.* **77**, 2222–2226.

Phan-Thien, N. & Antonia, R. A. 1994 Isotropic cartesian tensors of arbitrary even orders and velocity gradient correlation functions. *Phys. Fluids* **6**, 3818–3823.

Reynolds, W. C. & Hussain, A. K. M. F. 1972 The mechanics of an organised wave in turbulent shear flow. Part 3. Theoretical models and comparisons with experiments. *J. Fluid Mech.* **54**, 263–288.

Saddoughi, S.G. & Veeravalli, S. V 1994 Local isotropy in turbulent boundary layers at high Reynolds number. *J. Fluid Mech.* **268**, 333–372.

Schumacher, J., Sreenivasan, K.R. & Yeung, P.K. 2003 Derivatives moments in turbulent shear flows. *Phys. Fluids* **15**, 84–90.

Shen, X. & Warhaft, Z. 2000 The anisotropy of the small scale structure in high reynolds number ($R_\lambda = 1000$) turbulent shear flow. *Phys. Fluids* **12**, 2976–2989.

Siggia, E. D. 1981 Invariants for the one-point vorticity and strain rate correlation functions. *Phys. Fluids* **24**, 1934–1936.

Sreenivasan, K. R. & Antonia, R. A. 1997 The phenomenology of small-scale turbulence. *Ann. Rev. Fluid Mech.* **29**, 435–472.

Taylor, G. I. 1935 Statistical theory of turbulence. *Proc. Roy. Soc. London* **151 (873)**, 421–444.

Thiesset, F., Danaila, L., Antonia, R. A. & Zhou, T. 2011 Scale-by-scale energy budgets which account for the coherent motion. *J. Phys. Conference series ETC13, Warsaw* **318**, 052040.

Townsend, A.A. 1976 *The structure of turbulent shear flow*. Cambridge University Press.

Wygnanski, I., Champagne, F. & Marasli, B. 1986 On the large-scale structures in two-dimensional, small-deficit, turbulent wakes. *J. Fluid Mech.* **168**, 31–71.

Zhou, T. & Antonia, R. A. 2000 Reynolds number dependence of the small-scale structure of grid turbulence. *J. Fluid Mech.* **406**, 81–107.

Zhou, Y. & Antonia, R. A. 1994 Effect of initial conditions on vortices in a turbulent near wake. *AIAA J.* **32**, 1207–1213.

Zhou, Y. & Antonia, R. A. 1995 Memory effects in a turbulent plane wake. *Exp. Fluids* **19**, 112–120.